

POLYCRYSTALLINE SILICON SOLAR CELLS FABRICATED BY PULSED RAPID  
THERMAL ANNEALING OF AMORPHOUS SILICON

A Thesis

by

I-SYUAN LEE

Submitted to the Office of Graduate and Professional Studies of  
Texas A&M University  
in partial fulfillment of the requirements for the degree of  
MASTER OF SCIENCE

|                     |                  |
|---------------------|------------------|
| Chair of Committee, | Yue Kuo          |
| Committee Members,  | Zheng Dong Cheng |
|                     | Ohannes Eknayan  |
| Head of Department, | M. Nazmul Karim  |

May 2014

Major Subject: Chemical Engineering

Copyright 2014 Copyright I-Syuan Lee

## ABSTRACT

The PECVD intrinsic,  $n^+$ , and  $p^+$  a-Si:H thin film deposition processes have been studied by the optical emission spectroscopy to monitor the plasma phase chemistry. Process parameters, such as the plasma power, pressure, and gas flow rate, were correlated to  $\text{SiH}^*$ ,  $\text{H}_\alpha$ , and  $\text{H}_\beta$  optical intensities. The power, pressure, and hydrogen dilution effect on radical intensities and intensities ratio such as  $\text{H}_\alpha/\text{SiH}^*$  and  $\text{H}_\beta/\text{H}_\alpha$  were investigated. For all films, the deposition rate increases with the rise of the  $\text{SiH}^*$  intensity. For the doped films, the  $\text{H}_\alpha/\text{SiH}^*$  ratio is a critical factor affecting the resistivity. Changes of the free radicals intensities can be used to explain variation of film characteristics under different deposition conditions. The  $n^+$  and  $p^+$  layer were optimized by analyzing the optical emission spectra.

The  $i$ -layer was optimized by assembling it with  $n^+$  and  $p^+$  to a PIN diode and measuring the current-voltage characterization under solar light illumination.  $\text{H}_\alpha^*/\text{SiH}^*$  ratio is an important clue to study the effects of H content and Si-H binding mode on solar light conversion efficiency. The moderate hydrogenation can improve the film quality by passivating the dangling bonds, which acts like recombination centers in the film. However, too much H content leads to the increasing amount of  $\text{SiH}_2$  in the film, which causes the dangling bonds and deteriorates the film. The pattern size and the thickness of light-absorbed layer ( $i$ -layer) were also optimized.

The novel nickel-induced crystallization with low thermal budget was demonstrated. Polycrystalline silicon thin films were formed from the amorphous silicon

thin films by the pulsed rapid thermal annealing process enhanced with a thin nickel seed layer through the vertical crystallization mechanism. The crystalline volume fraction, grain size, and the material properties of polycrystalline  $i$ -,  $n^+$ , and  $p^+$  silicon layers were reported. The influence of PRTA frequency and the dopant effect were also investigated. It has been demonstrated that a 30 nm thick amorphous silicon could be transformed into polycrystalline with 70%-80% of crystalline volume fraction in a short time.

The thin-film polycrystalline silicon solar cells were produced using nickel-induced crystallization with amorphous silicon film and a thin Ni layer. The conversion efficiency was improved by transforming amorphous  $n^+$  to polycrystalline  $n^+$ . The  $n^+/i$ - and  $i/p^+$  interfaces trapped Ni atoms and deteriorated the diode property after crystallizing the films on the top of  $n^+$ . The current-voltage characterizations in the dark, under red, green, blue, and solar light illumination were measured and investigated.

## DEDICATION

To my parents and my sibling

## ACKNOWLEDGEMENTS

I would like to thank my advisor, Dr. Yue Kuo, for the opportunity for research at the Thin Film Nano and Microelectronics Research Laboratory and for the overwhelming guidance, training, and support the past two years. I'm indebted to my committee members, Dr. Zheng Dong Cheng and Dr. Ohannes Eknoyan for serving as members on my master committee.

Thanks also go to my colleagues: Chi-Chou Lin for the assistance with the sputtering and RIE machine, Kibum Kim for the assistance with the PECVD machine, Shu-Mao Chang for the metal deposition, and former colleagues: Dr. Helinda Nominanda and Shu-Hsien Wu for the technical discussions and friendships. I would like to thank the financial support from NSF project 0968862. I also appreciate the entire Chemical Engineering Department staff for the helpful assistance, Mr. Randy Marek and Mr. Jason Caswell for the assistance in repairing equipment.

Finally, I would like to dedicate this work to my family. The work could not be accomplished without their love and support.

## TABLE OF CONTENTS

|  | Page |
|--|------|
| ABSTRACT .....   | ii   |
| DEDICATION .....   | iv   |
| ACKNOWLEDGEMENTS .....   | v    |
| TABLE OF CONTENTS .....  | vi   |
| LIST OF FIGURES .....  | viii |
| LIST OF TABLES .....   | xi   |
| CHAPTER I INTRODUCTION AND LITERATURE REVIEW .....   | 1    |
| 1.1 Glow Discharge Film Deposition.....  | 1    |
| 1.2 A-Si:H Solar Cells and Poly-Si Solar Cells.....  | 3    |
| CHAPTER II EXPERIMENTAL METHODS .....  | 6    |
| 2.1 Fundamentals of Plasma.....  | 6    |
| 2.2 Plasma Enhanced Chemical Vapor Deposition (PECVD).....   | 8    |
| 2.3 Optical Emission Spectroscopy.....   | 11   |
| 2.4 Photonic Tools and System .....  | 12   |
| 2.5 Rapid Thermal Annealer .....   | 14   |
| 2.6 Raman spectroscopy.....  | 15   |
| CHAPTER III EMISSION SPECTRA STUDY OF PLASMA ENHANCED<br>CHEMICAL VAPOR DEPOSITION OF INTRINSIC AND HEAVILY DOPED<br>AMORPHOUS<br>SILICON..... | 17   |
| 3.1 Introduction.....  | 17   |
| 3.2 Experimental Method.....   | 18   |
| 3.3 Emission Spectra of Intrinsic a-Si:H Film Deposition.....  | 20   |
| 3.4 Emission Spectra of $n^+$ a-Si:H Film Deposition.....  | 26   |
| 3.5 Emission Spectra of $p^+$ a-Si:H Film Deposition.....  | 43   |

|   |    |
|---|----|
| CHAPTER IV PIN DIODE WITH AMORPHOUS SILICON UNDER SOLAR<br>LIGHT ILLUMINATION.....              | 52 |
| 4.1 Introduction.....   | 52 |
| 4.2 Experimental Method.....  | 52 |
| 4.3 The J-V Characteristics of a-Si:H Solar Cells.....  | 55 |
| 4.4 The Effect of Cell Size.....  | 60 |
| 4.5 The Effect of the Intrinsic Layer .....   | 61 |
| CHAPTER V POLYSILICON SOLAR CELL FABRICATION BY MULTIPLE<br>PULSED RAPID THERMAL ANNEALING..... | 69 |
| 5.1 Introduction.....   | 69 |
| 5.2 Experimental Method.....  | 69 |
| 5.3 Nickel-induced Crystallization of a-Si:H Thin Film by Multiple PRTA....                     | 73 |
| 5.4 Poly-Si Solar Cells Prepared by Nickel-Induced Crystallization.....                         | 83 |
| CHAPTER VI SUMMARY.....   | 90 |
| REFERENCES.....   | 96 |

## LIST OF FIGURES

| FIGURE  | Page |
|---|------|
| 1     Electron energy distribution in plasma and dissociation of silane molecule by impact of an electron .....   | 3    |
| 2     Simplified PECVD thin film deposition mechanism.....  | 7    |
| 3     Schematic of plasma-enhanced chemical vapor deposition system.....  | 9    |
| 4     Heating zones and reactor dimension.....  | 10   |
| 5     Measurement setup for solar cells.....  | 14   |
| 6     OES spectra for <i>i</i> -a-Si:H deposition under different conditions at 250°C.....  | 22   |
| 7     The dependence of deposition rate on SiH* intensity with (a) different power (b) different pressure.....  | 24   |
| 8     Power effects on (a) radicals intensities and (b) radicals intensities ratio. SiH <sub>4</sub> /H <sub>2</sub> / PH <sub>3</sub> (6.88% in H <sub>2</sub> ) 35/1000/20 sccm, 800 mT, and 250°C.....                       | 27   |
| 9     Power effect on the deposition rate and resistivity. SiH <sub>4</sub> /H <sub>2</sub> /PH <sub>3</sub> (6.88% in H <sub>2</sub> ) 35/1000/20 sccm, 800 mT, and 250°C.....   | 28   |
| 10    Hydrogen dilution effect on (a) radicals intensities, and (b) radicals intensities ratio. SiH <sub>4</sub> /H <sub>2</sub> / PH <sub>3</sub> (6.88% in H <sub>2</sub> ) 20-60/1000/20 sccm, 800 mT, 300 W, and 250°C..... | 32   |
| 11    Hydrogen dilution effect on the deposition rate and resistivity. SiH <sub>4</sub> /H <sub>2</sub> /PH <sub>3</sub> (6.88% in H <sub>2</sub> ) 20-60/1000/20 sccm, 300 W, 800 mT, and 250°C.....                           | 34   |
| 12    Pressure effect on (a) radicals intensities, and (b) radicals intensities ratio. SiH <sub>4</sub> /H <sub>2</sub> /PH <sub>3</sub> (6.88% in H <sub>2</sub> ) 60/1000/20 sccm, 300 W, and 250°C.....                      | 37   |
| 13    Pressure effect on the deposition rate and resistivity. SiH <sub>4</sub> /H <sub>2</sub> /PH <sub>3</sub> (6.88% in H <sub>2</sub> ) 60/1000/20 sccm, 300 W, and 250°C.....   | 38   |



|    |  |    |
|----|--|----|
| 14 | $n^+$ film resistivity vs. (a) $\text{SiH}^*$ , $\text{H}_\alpha^*$ , and $\text{H}_\beta^*$ intensities, and (b) $\text{H}_\alpha^*/\text{SiH}^*$ and $\text{H}_\beta^*/\text{H}_\alpha^*$ ratios. ....         | 41 |
| 15 | Power effects on (a) radicals intensities and (b) radicals intensities ratio. $\text{SiH}_4/\text{H}_2/\text{B}_2\text{H}_6$ (2% in $\text{H}_2$ ) 35/400/100 sccm, 800 mT, and 250°C.....                       | 45 |
| 16 | Power effect on the deposition rate and resistivity. $\text{SiH}_4/\text{H}_2/\text{B}_2\text{H}_6$ (2% in $\text{H}_2$ ) 35/400/100 sccm, 800 mT, and 250°C.....  | 46 |
| 17 | Hydrogen dilution effect on (a) radicals intensities, and (b) radicals intensities ratio. $\text{SiH}_4/\text{H}_2/\text{B}_2\text{H}_6$ (2% in $\text{H}_2$ ) 10-35/400/100 sccm, 450 mT, 500 W, and 250°C..... | 48 |
| 18 | Hydrogen dilution effect on the deposition rate and resistivity. $\text{SiH}_4/\text{H}_2/\text{B}_2\text{H}_6$ (2% in $\text{H}_2$ ) 10-35/400/100 sccm, 450 mT, 500 W, and 250°C.....                          | 49 |
| 19 | $p^+$ film resistivity vs. (a) $\text{SiH}^*$ , $\text{H}_\alpha^*$ , and $\text{H}_\beta^*$ intensities, and (b) $\text{H}_\alpha^*/\text{SiH}^*$ and $\text{H}_\beta^*/\text{H}_\alpha^*$ ratios.....          | 51 |
| 20 | (a) Cross-section view (b) Top-view of the a-Si:H PIN diode.....   | 54 |
| 21 | The $J$ - $V$ curves of the PIN diode in the dark and under solar light illumination.....  | 56 |
| 22 | Band diagrams of an unbiased p-n junction solar cell in the dark and under illumination.....   | 58 |
| 23 | The $J$ - $V$ curves of solar cells with optimized $n^+$ , $i$ -, $p^+$ films with different pattern size under solar light illumination.....  | 61 |
| 24 | The $J$ - $V$ curves of solar cells with different $i$ -layers.....  | 63 |
| 25 | Solar cell circuit model including the series and shunt resistances.....   | 64 |
| 26 | The efficiency of solar cells with different $i$ -layers vs. the $\text{H}_\alpha/\text{SiH}^*$ ratio from OES.....  | 67 |
| 27 | The normalized $V_{OC}$ , $J_{SC}$ , $FF$ , and efficiency vs. $i$ -layer thickness.....   | 68 |
| 28 | Process flow of the $a$ -Si:H crystallization by PRTA with a sacrificial $\text{SiO}_2$  | 70 |
| 29 | Process flow of poly-Si solar cell fabrication.....  | 72 |

|    |  |    |
|----|--|----|
| 30 | Microscope pictures of Ni-induced crystallization of (a) $n^+$ (b) $i$ - (c) $p^+$ .....   | 75 |
| 31 | Raman spectra of as-deposited $i$ -layer and the $i$ -layers after 1-4 cycles<br>PRTA treatments.....  | 77 |
| 32 | Raman spectra of (a) as-deposited $n^+$ layer and the $n^+$ layers after 1-3<br>cycles PRTA treatments, and (b) as-deposited $p^+$ layer and the $p^+$ layers<br>after 1-3 cycles PRTA treatments.....   | 78 |
| 33 | J-V curves of solar cells with a-Si:H and poly-Si films prepared by NIC<br>under solar light illumination, (a) all a-Si:H, (b) $n^+$ -layer crystallized by<br>NIC, (c) $i$ - $n^+$ layers crystallized by NIC, and (d) $p^+$ - $i$ - $n^+$ layers crystallized<br>by NIC..... | 84 |
| 34 | $J$ - $V$ curves of the all a-Si:H diode and the poly-Si $n^+$ diode prepared by<br>NIC, (a) under red light illumination, (b) under green light illumination,<br>(c) under blue light illumination, and (d) in the dark.....  | 88 |

## LIST OF TABLES

| TABLE  | Page |
|--|------|
| 1 $(R_s)$ of the solar cells with different $i$ -layer.....  | 63   |
| 2     The grain sizes ( $L$ ) and the crystalline volume fraction ( $X_c$ ) of $p^+$ , $n^+$ and $i$ - Si samples..... | 80   |
| 3     The sheet resistivity of $p^+$ and $n^+$ samples.....  | 82   |
| 4     Cell performance of all a-Si:H and NIC samples.....  | 85   |

# CHAPTER I

## INTRODUCTION AND LITERATURE REVIEW

### 1.1 Glow Discharge Film Deposition

Hydrogenated amorphous silicon (a-Si:H) has been recognized as a useful thin-film semiconductors for opto-electronic-device applications such as solar cells, thin film transistor, etc [1, 2]. Usually a-Si:H film should be prepared by radio-frequency plasma enhanced chemical vapor deposition (RF-PECVD) technique with  $\text{SiH}_4$  gas. The process of PECVD glow discharge plays an important role in a-Si:H film deposition and determines the structure and property of the film. Therefore, it is very important to diagnose the process of glow discharge for optimizing deposition conditions. RF glow discharge in  $\text{SiH}_4$  have been investigated with diagnostic techniques such as mass spectrometry [3], optical emission spectroscopy (OES) [4], Langmuir probe [5], and reflection high-energy electron diffraction [6]. In a RF glow discharge process, high energy electrons accelerated by the electric field cause initial ionization and dissociation of  $\text{SiH}_4$ , producing primarily  $\text{SiH}_n$  radicals, H and  $\text{H}_2$ , but also  $\text{SiH}_n^+$  and  $\text{H}_n^+$  ions and secondary electrons, as shown in figure 1 [7]. The majority of the glow discharges produce mostly neutral fragments of the  $\text{SiH}_4$ , and the diffusional mass transport of the neutral radicals is important for the growth of a-Si:H [8]. Since the mean electron density of order of  $10^{10} \text{ cm}^{-3}$  in the plasma appears to be insufficient to produce a high density of ionic species, the generation of neutral radicals is much more than the ionization state [8]. Among these techniques, OES has a great advantage to make direct

observation of neutral radicals, and minimal influence on the plasma. It provides information about the reactive precursors and radicals, such as SiH, H<sub>2</sub>, and H [9].

Species that are reactive with silane form stable higher-order silane or heavier radicals, which eventually gather into silicon clusters or particles. Surviving neutral radicals and positive ions reach the surface and grow the a-Si:H film [7]. Atomic hydrogen also reaches the surface and be able to extract lightly bonded SiH<sub>3</sub> radicals from the surface. High energy positive ions can bombard the surface, leading to sputtering of the film, and low energy ions might bond to the film just like neutral radicals [9]. By varying the deposition condition such as power, pressure, and gas flow rate, the intensity of radicals may change and the film property can be altered.

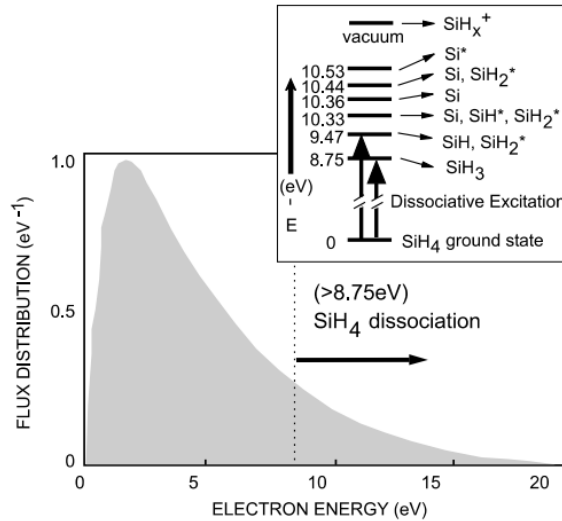


**Figure 1.** Electron energy distribution in plasma and dissociation of silane molecule by impact of an electron [7].

## 1.2 A-Si:H Solar Cells and Poly-Si Solar Cells

The development of silicon solar cells has been quickly progressed since the first thin-film silicon solar cell based on hydrogenated amorphous silicon (a-Si:H) was reported in 1976 [10]. In the last decade, a lot of research about single- and multi-junction solar cells and large-area modules based on a-Si:H and related alloys (e.g., a-Si<sub>1-x</sub>Ge<sub>x</sub>:H) have been reported. Even though the amorphous material has lower charge carrier mobility and diffusion length due to the disordered structure, the passivation of the potential defects by hydrogen makes this material more stable than other materials. Besides, the a-Si:H can be deposited at low temperature and be stacked without constraints because of its noncrystalline structure [11]. The doping of a-Si:H can be easily achieved by adding dopant gas during the deposition. The great flexibility of this material makes it more attractive for application of large-area thin-film electronics. For example, in addition to solar cells, a-Si:H has been used in many application such as Thin Film Transistor (TFT), sensors, and other opto-electronics devices [1, 2].

With the larger band gap of a-Si:H (1.7-1.9 eV), higher open-circuit voltages can be achieved in solar cells compared with that of the crystalline silicon (c-Si) (1.1 eV) [12]. However, the photocurrent is limited due to the insufficient light absorption of the solar cell spectrum. Also, light-induced degradation of a-Si:H can limit the conversion efficiency [11]. Compared with a-Si:H thin film solar cells, the polycrystalline silicon (poly-Si) thin film cells have additional advantages of high conversion efficiency, longer lifetime, and improved stability [11]. J.-D Hwang *et al.* reported a high conversion efficiency poly-Si solar cell formed from a-Si without passivation or antireflection layers,

with a conversion efficiency of 10.4% [13]. Poly-Si has the grain size in the range of 1  $\mu\text{m}$  to 1 mm. Thin-film poly-Si can be produced in various ways; however, all the processes take a long time ( $> 10$  hours) or need relatively high processing temperatures (between  $400^\circ\text{C}$  and  $1200^\circ\text{C}$ ), such as chemical vapor deposition (CVD), solid phase crystallization, or metal-induced crystallization [14, 15]. Previously, Kuo *et al.* demonstrated that a-Si thin film could be crystallized with a novel pulsed rapid thermal annealing (PRTA) process that exposed the sample to one or several short heating-and cooling cycles [16-18]. The glass substrate remain flat without warping or cracking after the crystallization process due to the low thermal budget of the process. A critical element of the PRTA process is the Ni-induced crystallization mechanism. Since the Ni residue in the film is undesirable, it has to be removed. It was reported that the sacrificial  $\text{SiO}_2$  formed on top of the a-Si surface can trap the Ni. After stripping off the Ni-containing  $\text{SiO}_2$  layer, the Ni residue in the crystallized layer was reduced.

The authors investigated the influence of the PRTA frequency on the undoped and doped Si layer with the inclusion of the  $\text{SiO}_2$  sacrificial layer. The application of crystallization method on Si solar cell was reported.

## CHAPTER II

### EXPERIMENTAL METHODS

#### 2.1 Fundamentals of Plasma

In PECVD, plasma is generated by RF power applied between two parallel electrodes. The top electrode is powered and the bottom electrode and the wall are grounded. The applied RF power is a varying electric field in which a free electron can be accelerated to collide with an atom or molecules to generate negative and positive charges. Due to the partial ionization state, the plasma is a quasi-neutral gas including neutral (radicals), negative (electrons), and positive charges (ions). The atoms or molecules are activated to an excitation state by the electron hit, then relax to ground state and emit photon, which can be detected and analyzed by optical emission spectroscopy (OES).

The ion bombardment energy in the plasma is resulted from the potential drop between the electrode and plasma. Because electron thermal velocity is about 100 times the ion thermal velocity, the fast-moving electrons are free in all direction, and will be lost to the grounded wall and bottom electrode shortly. Then, a positively charged space, called sheath region, is formed on the finite distance from the electrode, resulting in a potential drop from the plasma to both electrodes. Therefore, the electric field across the sheath region repels the electrons into the plasma and attracts the ions from the plasma into electrodes, leading to the ion bombardment [19].



Figure 2 shows a simplified diagram of a plasma thin-film process. The mechanism of plasma deposition can be divided into 7 steps: 1. Transport of reactants to the deposition region by force convection. 2. The gas species from the main gas stream through the boundary layer to the substrate. 3. The absorption of reactants at the substrate. 4. Surface processes, including chemical reaction, surface migration, site incorporation, and other surface reactions. 5. Desorption of the byproduct from the surface. 6. The diffusion of byproduct through the boundary layer. 7. Transport of byproduct away from the deposition region by force convection. [20, 21]

The process parameters such as power, pressure, gas flow rate, and substrate temperature can affect the plasma behavior. For example, gas pressure determines the gas residence time and consumption time at the substrate. RF power and frequency are responsible for the plasma density and ion bombardment energy.

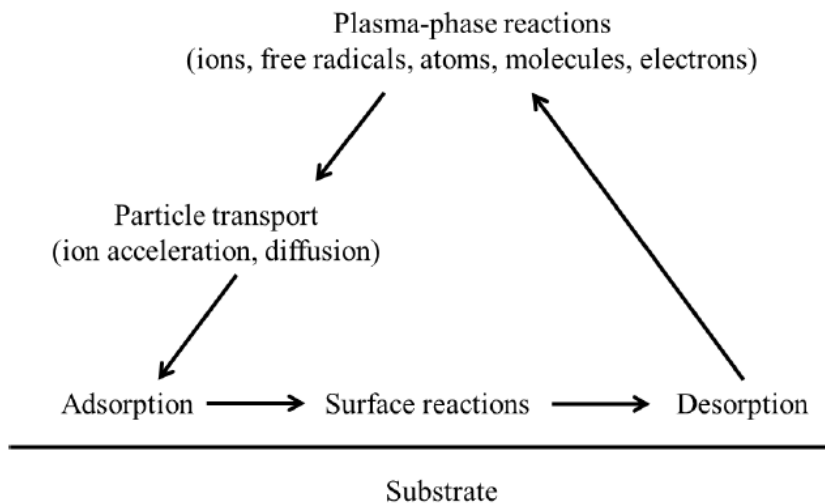


**Figure 2.** Simplified PECVD thin film deposition mechanism. [20]

## 2.2 Plasma-Enhanced Vapor Deposition (PECVD)

Plasma enhanced chemically vapor deposited (PECVD) a-Si:H thin films have been widely used in thin film Parallel plate PECVD reactor (Applied Material, AMP Plasma I) was used to deposit a-Si:H, heavily doped  $n^+$ ,  $p^+$  a-Si:H films. Figure 3 shows the simplified schematic of PECVD chamber with all of its main features and control system. The mass flow controllers are used to control the radial gas flow system. The pressure control system includes an angle valve, a booster pump, and a mechanical pump, and capacitor manometer (pressure sensor). The temperature system is made of three-zone heater and controllers. The plasma system consists of the 13.56 MHz RF generator (OEM-12A, ENI), a pi-type matching network (MW-10, ENI), and a plasma controller. The top electrode of the PECVD chamber was powered and the bottom electrode and the wall were grounded. The pressure, plasma and mass flow control systems are controlled by PC with LabWindow/CVI interface (National Instrument).

The gas supply into the reactor through the mass flow controllers include: N<sub>2</sub> (ultra high purity, Acetylene Oxygen Company), N<sub>2</sub> (semiconductor, 99.9999% purity, Praxair), Ar (semiconductor, 99.9999% purity, Praxair), SiH<sub>4</sub> (semiconductor, 99.999% Air Liquide), B<sub>2</sub>H<sub>6</sub> (2 % in H<sub>2</sub>, 99.999% purity, Air Liquide), PH<sub>3</sub> (7.1 % in H<sub>2</sub>, 99.999%, Air Liquide), NH<sub>3</sub> (semiconductor, 99.999% purity, Matheson Tri-Gas), and H<sub>2</sub> (semiconductor, 99.9999% purity, Praxair). Figure 4 shows the heating zones and the dimension of the reactor chamber. The substrate was placed in the same position on the center zone during each deposition to ensure the consistent deposition rate.

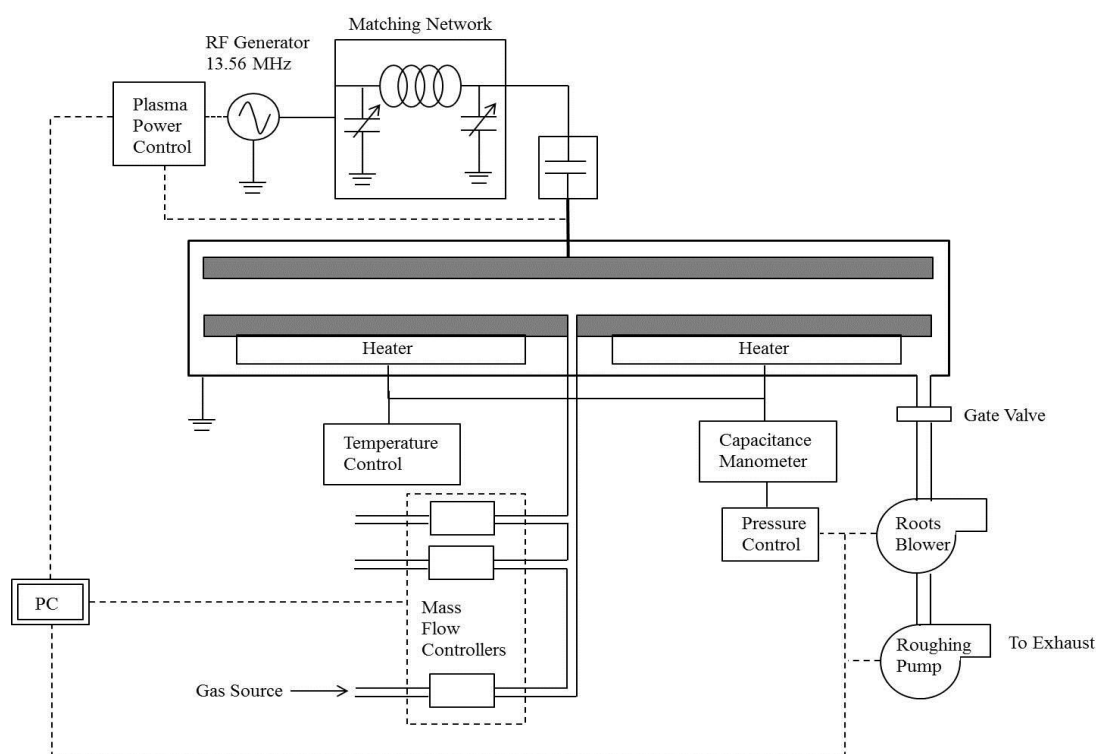


**Figure 3.** Schematic of plasma-enhanced chemical vapor deposition system.

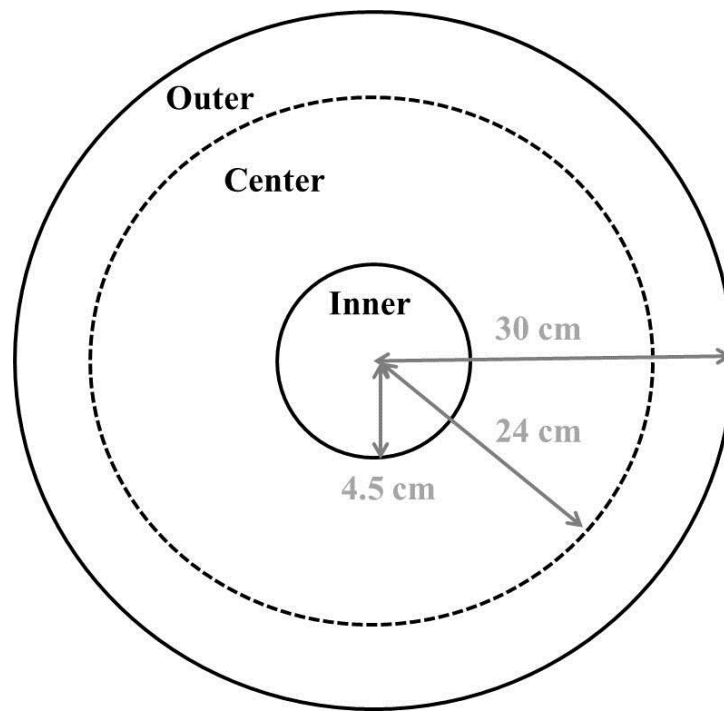


**Figure 4.** Heating zones and reactor dimension.

## 2.3 Optical Emission Spectroscopy

During PECVD deposition, the atoms or molecules are activated to an excitation state by the electron hit, then immediately relax to ground state and emit photon, which can be detected and analyzed by optical emission spectroscopy (OES). The OES (StellarNet Black-Comet-C-SR) is a method of chemical analysis that uses the intensity of light emitted from plasma at a particular wavelength to determine the quantity of an element in a sample. The wavelength of the optical spectral line can be used to identify the element while the intensity of emitted light is proportional to the number of atoms or molecules of the element. The light-emitted elements usually includes activated atom (e.g. H) or activated molecules (mostly binary molecules e.g. H<sub>2</sub>). The activated ions (e.g. Al<sup>+</sup>) or polyatomic molecules emit much weaker light. Since radicals are usually the intermediate reactant, the diagnosis of OES provides the information of intermediate chemical reaction. Besides, the intensity of light can be affected by deposition parameters (power, pressure, temperature, etc.) and precursor concentration. StellarNet's miniature fiber optic spectrometers, which utilize a 40 mm diameter concave grating with aberration correction, deliver high performance for spectroscopy application in the UV-VIS wavelength ranges covering 200-1100 nm. The concave grating produces a flat field on the CCD detector creating uniform resolution over the entire range. To get rid of the error near the wavelength limit, spectra are collected in the 300-800 nm range. Before the plasma is generated, all the intensities are set to almost 0 by deducting the background. After the plasma is generated, all the intensities start from 0, and the intensities in different conditions are only affected by the system factor. The sensor is

attached on the PECVD window tightly without any interference from surrounding light. The spectrum was collected after the plasma was turned on for 1 minute to make sure that the plasma is steady. The OES can only detect light-emitted elements in the plasma. Other elements which do not emit light should be diagnosed by mass spectrometer or FTIR.

## **2.4 Photonic Tools and System**

The full spectrum (AM1.5) solar light is generated by a solar light simulator (16S-300-002, Solar Light Co., Inc.) with a vertical beam adaptor that redirects the light beam to point downward. The spot size is typically 2.25 inches with 1 sun output intensity ( $1000 \text{ W/m}^2$ ). By varying the current using the control knob on the power supply, the intensity can be varied between 80% and 100% of maximum. The solar light intensity is tested by a PMA 2144 pyranometer and a calibrated PMA 2100 dose control system (Solar Light Co., Inc.). It is based on thermopile technology assuring very broad spectral sensitivity with exceptional flatness and long term stability. Heating of the sensor by solar radiation produces a signal in the  $\mu\text{volt}$  range, which can be transferred to the radiant power by its own calibration factor and the processing algorithm. The sensor has an optical glass dome on the top which acts as a filter, allowing the full solar spectrum to pass through it. It also protects the sensor from the elements. The sensor is

ready to operate few seconds after plugging to the connector on the power meter. Figure 5 shows the measurement setup of this study. The sensor has a height of 8.4 cm. Therefore, the sample holder was raised up at the same height to make sure the calibration accuracy. The sample was placed in the middle of solar light spot. To obtain the consistent power, the power density of solar light was calibrated by the pyranometer before each measurement. The power intensity was fixed at  $1000 \text{ W/m}^2$ .

The mono-wavelength light is introduced by using different LEDs, M625L2, M530L2 and M470L2 from Thorlabs, i.e., red at 625 nm, green at 530 nm, and blue at 470 nm. The photon energies of the red, green, and blue LEDs are 1.98 eV, 2.34 eV, and 2.64 eV separately which are larger than the band gap energy of a-Si:H i.e., 1.7 eV. The power density of the LED was fixed at  $28.4 \text{ W/m}^2$ .

The  $J$ - $V$  measurements were carried out using the Agilent 4140B parameter analyzer in a sweep mode with increment of 0.01 V. All measurements were made in the probe station in a black box.

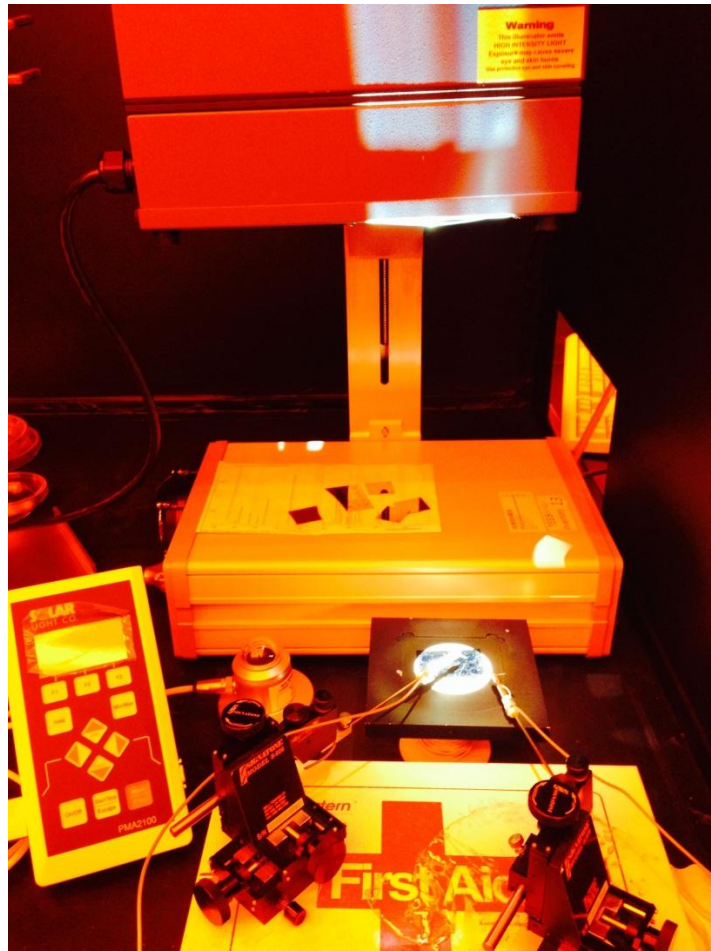


**Figure 5.** Measurement setup for solar cells.

## **2.5 Rapid Thermal Annealer**

The rapid thermal annealer (RTA, REP600S, Modular Process Tech. Corp.) features quartz chamber, quartz tray, and highly uniform lamp array which can raise the chamber temperature in the range of 250-1300 °C in the rate of 0-200 °C/sec with multi-gas capabilities. The temperature measurement techniques for RTP-600S are thermocouple and pyrometer. The type K thermocouple is useful for low-temperature



processing and calibrating the pyrometer. The Extended Range Pyrometer Plus (ERP+) pyrometer can be used to measure water temperature in the range of 350-1250°C. An integrated software package features real-time process control, graphics display, and data collection has a comprehensive diagnostic function.

The pulsed rapid thermal annealing (PRTA) process is used to crystallize a Ni-contacted a-Si thin film into a poly-Si thin film. It is based on the principle of exposing substrate to short heating-cooling cycles repeatedly, i.e. 10 cycles with each cycle composed of 1 sec of 850°C heating and 5 sec of cooling under the N<sub>2</sub> ambient in this experiment. The cooling cycle was done by turning off the heater and introducing the cooling water. The actual minimum temperature in the cooling cycle was about 530°C after the first cycle and slightly higher in subsequent cycles. After all cycles, the sample was cooled down to room temperature under the N<sub>2</sub> ambient for approximately 20 min.

## **2.6 Raman Spectroscopy**

Raman spectroscopy (Renishaw System 2000, Ar ion laser Coherent Innova 70, Leica INM 200) utilizes the inelastic scattering of photons from incident light of a monochromatic laser onto the substrate [22]. The molecule is excited from ground state to a virtual energy state by an incident photon, then the molecule returns to a different rotational or vibrational state and emits a photon. There are three major types of photon scattering: Raleigh, Raman Stokes, and Raman Anti-Stoke. If the final vibrational state of molecule has higher energy than that of initial state, the emitted photon will be shifted to lower frequency due to the total energy balance in the system. This shift in frequency

is named the Stokes shift. If the final vibrational state has lower energy, the emitted photon will be shifted to a higher frequency, and this is named an anti-Stokes shift. If the final vibrational state has the same energy as the initial state, it is named Rayleigh scattering. The Raman shift is represented by the more intense Raman Stokes scattering. The photodetector detects the photon frequency shift by the Raman Stokes. A plot of the signal intensity at a range of Raman shift then can be obtained.

Raman spectroscopy can be used to quantify and qualify the amount of amorphous and crystalline phase at the Si films. The peak around  $520\text{ cm}^{-1}$  corresponded to single crystalline Si (c-Si), the peak between  $510\text{ cm}^{-1}$  and  $515\text{ cm}^{-1}$  indicates the grain boundary in polycrystalline Si (poly-Si), and the broad peak near  $490\text{ cm}^{-1}$  is contributed by the amorphous phase. The irregularity of the amorphous phase causes the broad Raman Stokes intensity. The crystallinity of the Si film can be quantified by the ratio of the crystalline and amorphous peaks [23].

## CHAPTER III

### EMISSION SPECTRA STUDY OF PLASMA ENHANCED CHEMICAL VAPOR DEPOSITION OF INTRINSIC AND HEAVILY DOPED AMORPHOUS SILICON

#### 3.1 Introduction

Plasma enhanced chemically vapor deposited (PECVD) a-Si:H thin films have been widely used in thin film transistors (TFTs), *p-i-n* diodes, solar cells, optoelectronic devices, etc. [1,2]. Process parameters, such as the power, pressure, temperature, and feed gas stream, affect the deposition rate and electrical properties of the film. The optical emission spectroscopy (OES) is a powerful diagnosis tool to characterize the PECVD process [9]. For example, for the a-Si:H deposition using the SiH<sub>4</sub>/H<sub>2</sub> feed stream, excited species such as SiH\* (414 nm), H <sub>$\alpha$</sub> \* (656 nm), and H <sub>$\beta$</sub> \* (486 nm) are important components in the plasma phase. It was reported that the H <sub>$\alpha$</sub> \*/SiH\* intensity ratio could be related to the crystallinity in the film [24]. In addition, the H <sub>$\beta$</sub> \*/H <sub>$\alpha$</sub> \* ratio could be used to estimate the electron temperature [25]. The high T<sub>e</sub> favors the  $\mu$ c-Si:H formation. However, when the T<sub>e</sub> is too high, it leads to instability of the film's microstructure [26].

In this chapter, the optical emission scope (OES) is used to monitor the plasma phase chemistry during PECVD thin film depositions. Changes of the SiH\*, H <sub>$\alpha$</sub> \*, and H <sub>$\beta$</sub> \* OES intensities with respect to the plasma power, pressure, and feed gas flow rate are investigated. For the doped film, the relationship between the free radical intensity and the resistivity is studied.

The  $i^-$ ,  $n^+$ , and  $p^+$  a-Si:H thin films were deposited with a PECVD system at 13.56 MHz plasma frequency. The OES with a spectral range 250-800 nm was used to monitor the plasma during the deposition.

### 3.2 Experimental Method

The PECVD system (Applied Materials, AMP Plasma I) that had a parallel-electrode design was used to deposit  $i^-$ ,  $n^+$ , and  $p^+$  a-Si:H thin films. The top electrode was driven by 13.56 MHz RF power generator with an automatic matching box. The PECVD chamber and the electrode were cleaned by isopropanol alcohol and diluted HF after 4  $\mu\text{m}$  of the deposited film has been accumulated. The Corning 1737 glass was used as the substrate for the silicon films. The cleaning procedure was as follow. First, the glass was immersed in de-ionized (DI)  $\text{H}_2\text{O}$  ( $> 18 \text{ M}\Omega\text{-cm}$ ) with ultrasonic cleanser for 10 minutes. Second, the substrate was rinsed by acetone to minimize the contaminants. Third, the isopropanol alcohol was used to remove the acetone on the substrate. Finally, a large amount of water was used to rinse the glass, and the substrate was immediately dried with air gun. Before each deposition, the glass was dipped in dilute HF (1%) for several seconds to remove the native oxide, and a 2000  $\text{\AA}$   $\text{SiN}_x$  as an adhesion layer was precoated at 300 W, 500 mT at 250  $^\circ\text{C}$  for 14 minutes by PECVD. The feed stream was composed of 20 sccm  $\text{SiH}_4$ , 600 sccm  $\text{N}_2$ , and 80 sccm  $\text{NH}_3$ . After the substrate was loaded to the heated PECVD chamber, the chamber is pumped down to 1 mT by the combination of roughing pump and blower. It was followed with the 2 times of purging and pumping with Ar.

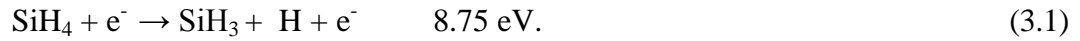
Systematic independent depositions at 250 °C were performed to observe the effect of various process parameters such as pressure, power, and gas flow rate. The pressure range was 150-800 mT and the power range was 80-500 W. For the *i*-layer deposition, SiH<sub>4</sub> was used as the feed gas. For the *n*<sup>+</sup> film deposition, the feed stream was composed of SiH<sub>4</sub> (10-60 sccm), H<sub>2</sub>, (400-1000 sccm), and PH<sub>3</sub> (6.88% in H<sub>2</sub>) (1-20 sccm). For the *p*<sup>+</sup> film deposition, the feed stream was composed of SiH<sub>4</sub> (10-35 sccm), H<sub>2</sub> (400-1000 sccm), and B<sub>2</sub>H<sub>6</sub> (2% in H<sub>2</sub>) (10-100 sccm). Each film was deposited at least 15 minutes to make sure the thickness was higher than 2000 Å. Film thickness was obtained from the step height measured with a stylus profilometer (Dektak 3, Veeco Instrument). The sharp step was formed by the wet etching process. The film was coated with the black wax, and the uncoated area was etched. Then the step was formed after removing the wax with xylene. For *i*- layer, the uncoated area was etched with dilute HF (2%). For *n*<sup>+</sup> film, the uncoated area was etched with dilute KOH (KOH: DI H<sub>2</sub>O=1:10, weight %) For *p*<sup>+</sup> film, the film was coated with photoresist in certain area, and the uncoated area was etching by reactive ion etching (RIE) (700C, Plasma Therm) using 20 sccm CF<sub>4</sub> at 100 mT, 300 W for about 20 minutes. The deposition rate was calculated by dividing the film thickness over deposition time. The film's resistivity was determined from a 4-point probe (Alessi Industry).

During the deposition, the emission spectrum in the 300-800 nm range was monitored using an OES (StellarNet Black-Comet-C-SR). Before the plasma was generated, all the intensities were set to almost 0 by deducting the background. After the plasma was generated, all the intensities started from 0, and the intensities in different

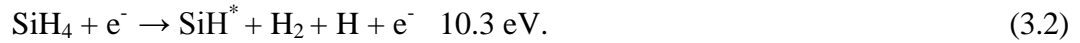
conditions were only affected by the system factor. The spectrum was collected after the plasma was turned on for 1 minute.

### 3.3 Emission Spectra of Intrinsic a-Si:H Film Deposition

For a a-Si:H deposition,  $\text{SiH}_3$  is considered to be the predominant growth precursor for the growth of a-Si:H.  $\text{SiH}_3$  is a reaction product of electron impact dissociation of  $\text{SiH}_4$  [7], e.g.



Dissociation of  $\text{SiH}_4$  also leads to excited states  $\text{SiH}^*$ , e.g.



The intensity of the emission line  $I(\text{SiH}^*)$  is proportional to the concentration  $[\text{SiH}^*]$ , which is determined by the dissociation rate of  $\text{SiH}_4$ . Therefore, even though the weak or non-emissive radicals ( $\text{Si}_x\text{H}_y$ ,  $x, y \geq 2$ ) are not easy to detected and determined their density by OES, the  $I(\text{SiH}^*)$  still gives some information about the deposition process.  $I(\text{SiH}^*)$  is given by

$$I(\text{SiH}^*) \propto [\text{SiH}_4] N_e. \quad (3.3)$$

Where  $N_e$  is the electron density with an energy above the threshold energy. Dissociation of molecular hydrogen  $\text{H}_2$  by an electron impact can lead to  $\text{H}^*$  by



The reaction is followed by  $H_\alpha$  Balmer emission  $H^*(n=3 \rightarrow 2)$  and  $H_\beta$  Balmer emission  $H^*(n=4 \rightarrow 2)$  [27, 28]. The  $H^*$  concentration is proportional to the  $H_2$  concentration and the density of electrons above the energy threshold. For example,  $I(H_\alpha)$  is given by

$$I(H_\alpha^*) \propto [H_2] N_e. \quad (3.6)$$

Figure 6 shows the emission spectra of different intrinsic a-Si:H film deposition conditions. The  $SiH_4$  is the only feeding gas and the flow rate is kept constant (50 sccm) in all conditions. There are several major spectral peaks, i.e.,  $SiH^*$  (414 nm),  $H_\alpha^*$  (656 nm), and  $H_\beta^*$  (486 nm). The intensities of those species were used as references of their concentration. The actual species concentration in the plasma phase can be estimated with the actinometry method [29]. All the intensities are divided by the maximum intensity, i.e. the maximum intensity of  $SiH^*$  in the condition of 50 sccm, 200W, 500mT. Therefore, all the intensities are in the range between 0 and 1. The intensities of  $SiH^*$ ,  $H_\alpha^*$ ,  $H_\beta^*$ , and  $H_2$  increase with the rise of power, e.g., 100 W vs. 200 W at  $SiH_4$  50 sccm and 400 mT. However, when the power is low or the pressure is high, e.g. at 80 W and 150 mT or 100 W and 500 mT, only the  $SiH^*$  is detected, and the intensity of  $SiH^*$  is much lower than that in other conditions. The low intensity of  $SiH^*$  and almost 0 intensity of H reveal the low dissociation rate of  $SiH_4$ . The  $SiH_4$  plasma contains a large amount of atomic hydrogen that plays a dual role in the film formation process, i.e., to passivate the dangling bonds or to etch the weak Si-Si bond [30, 31]. The low power or high pressure deposited film may contain many weak Si-Si and unsaturated dangling bonds, which affects the device performance. However, high concentration of hydrogen

leads to serious positive ion bombardment, which will cause damage in the film structure. The formation of a less dense a-Si:H network with voids deteriorates the electronic properties [31]. For example, the *p-i-n* solar cell prepared from the low power or high pressure *i*-layer (e.g. 80 W/150 mT and 100 W/500 mT) has the lower conversion efficiency than those of cells with the *i*-layers deposited from other conditions. However, the solar cell prepared from the condition with the highest  $H_a^*/SiH^*$  ratio (e.g. 200 W/400 mT) also has inferior efficiency.

It was reported that the  $H_a^*/SiH^*$  intensity ratio was related to the crystalline phase formation in the PECVD  $\mu c$ -Si:H film [24]. When the  $H_2$  concentration is over 97%, the crystalline phase forms [32]. Since the feed streams of Fig. 1 samples contain no  $H_2$ , the deposited films are amorphous as confirmed with the Raman spectroscopy, i.e., only a broad feature near  $480\text{ cm}^{-1}$  [32].

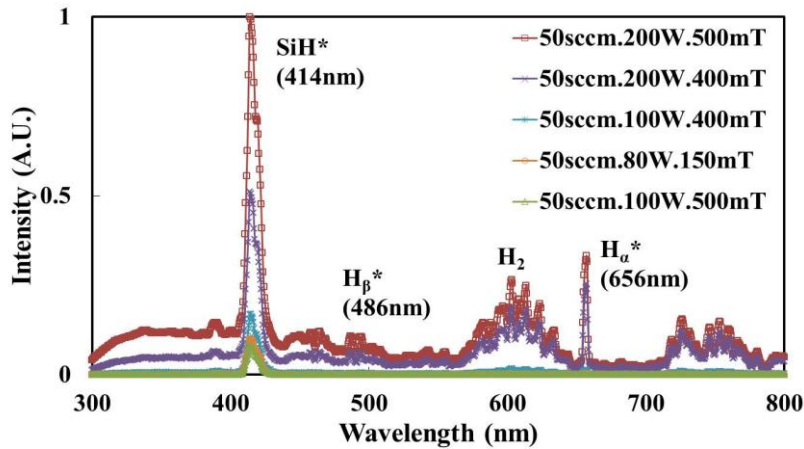
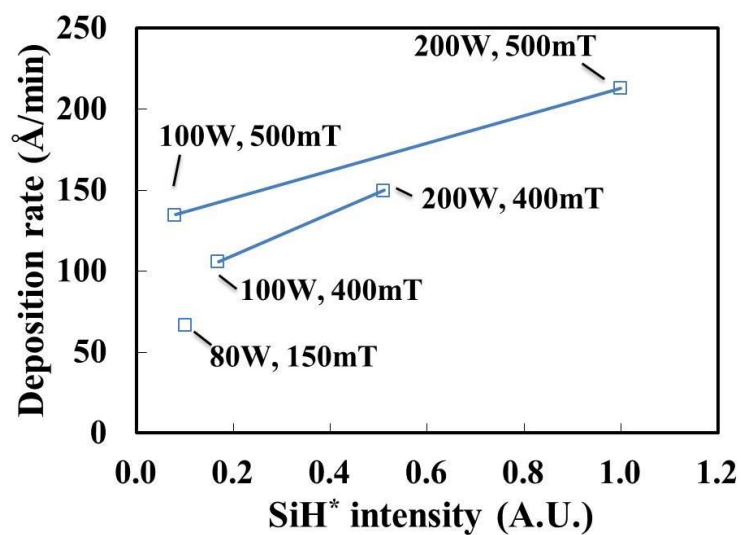


**Figure 6.** OES spectra for *i*- a-Si:H deposition under different conditions at 250°C.

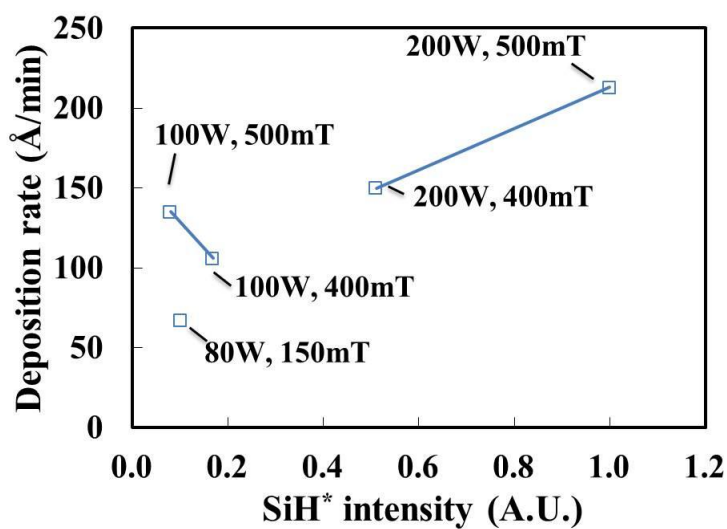


Figure 7 shows the dependence of deposition rate on the  $\text{SiH}^*$  intensity with different power and pressure. The  $\text{SiH}^*$  intensity increases with the increase of power. The increase of power promotes both the electron density and electron temperature [26]. Therefore, it contributes to the increasing amount of electrons above the energy threshold ( $N_e$ ), leading to the generation of large amount of  $\text{SiH}^*$ . The deposition rate increases with the increase of  $I(\text{SiH}^*)$ . In addition, the power effect is more evident in high pressure.

In addition, influences of pressure on the  $\text{SiH}^*$  is dependent on the magnitude of power. With 100 W of power, the  $\text{SiH}^*$  increases with the decreases of pressure. With 200 W of power, the result is in opposite trend. Plasma modeling showed that the  $\text{SiH}_4$  density increases with the increasing pressure [32]. Due to the increasing chances of collisions, the electron density distribution shifts to lower energy, leading to a reduction of  $N_e$  with an energy above the threshold energy. Considering these changes, with the increasing pressure, the increase of  $[\text{SiH}_4]$  and the decrease of  $N_e$  compete with each other in determining  $I(\text{SiH}^*)$ . For example, for the low power condition (100 W), the reduction of  $N_e$  is probably higher compared to the increase of  $[\text{SiH}_4]$ , resulting in the much lower  $I(\text{SiH}^*)$  with the increasing pressure. For the high power condition (200 W), the reduction of  $N_e$  is compensated by the power promotion, plus the increase of  $[\text{SiH}_4]$ , resulting in the increase of  $I(\text{SiH}^*)$  with the increasing pressure.



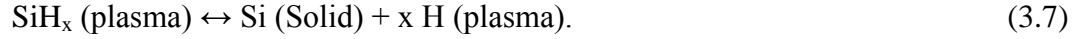
(a)



(b)

**Figure 7.** The dependence of deposition rate on  $\text{SiH}^*$  intensity with (a) different power (b) different pressure.

In the SiH<sub>4</sub> plasma, the dissociation and recombination mechanisms affect the film deposition phenomena [33]. Since plasma deposition of a-Si:H from SiH<sub>4</sub> is a rather complicated process, the net reaction can be simply expressed by the following equation [30]:

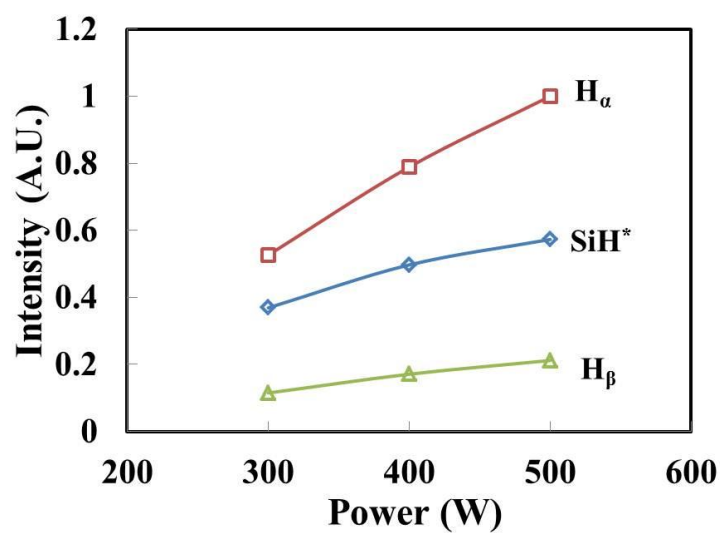


In the normal deposition condition, the reaction is predominantly forward, resulting in dissociation and, hence, the film formation. However, even in undiluted SiH<sub>4</sub> condition, the reverse reaction also takes place, which leads to H etching of the growing surface. With increasing pressure, the dissociation rate is determined by the competition between the increase of [SiH<sub>4</sub>] and the reduction of electron energy, and the recombination rate is determined by the competition between the increase of [H<sub>2</sub>] and the reduction of electron energy. Based on this, the dependence of deposition rate on pressure should not have a single trend in this case.

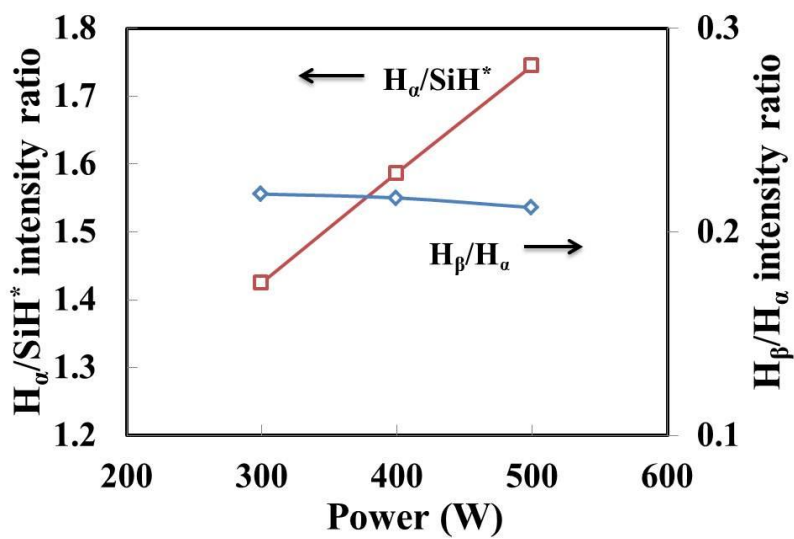
### 3.4 Emission Spectra of $n^+$ a-Si:H Film Deposition

#### 3.4.1 Power Effect

In the  $n^+$  a-Si:H deposition processes, the optical emission from the PH (342 nm) and P lines (214, 215, 253, and 255 nm) could not be detected most likely due to the low dopant gas concentration in the feed gas stream, e.g., 0.01%-0.13% for  $\text{PH}_3$ . The  $\text{SiH}^*$ ,  $\text{H}_\alpha^*$ ,  $\text{H}_\beta^*$ , and  $\text{H}_2$  concentrations in the  $\text{SiH}_4/\text{H}_2/\text{PH}_3$  plasmas are almost the same as those in the  $\text{SiH}_4/\text{H}_2$  plasma. Figure 8(a) shows the power effect on the radical intensities at  $\text{SiH}_4/\text{H}_2/\text{PH}_3$  35/1000/20 sccm, 800 mT, 250°C. All intensities increase with the increase of power. For example, the  $\text{SiH}^*$  and  $\text{H}_\alpha^*$  intensities at 500 W are 1.55 and 2 times those at 300W, separately. It reveals the  $\text{SiH}_4$  dissociation rate is enhanced with the increase of the power. The increase of the  $\text{H}_\alpha^*$  intensity is more obvious than the increase of the  $\text{SiH}^*$  intensity. Figure 8(b) shows that the  $\text{H}_\alpha^*/\text{SiH}^*$  ratio increases with the rise of power. It is because that  $\text{H}_2$  can be contributed by the dissociated  $\text{SiH}_4$  and the feed gas, but  $\text{SiH}^*$  can only be formed from of the dissociated  $\text{SiH}_4$ . G.J. Nienhui *et al* reported that the  $\text{H}_\beta^*/\text{H}_\alpha^*$  ratio can be used to estimate electron temperature [32]. Since the  $\text{H}_\beta^*/\text{H}_\alpha^*$  ratio in Fig. 3(a) is independent of the power, the  $T_e$  is not influenced by the increase of power. Therefore, in this case, the increase of the power mainly contributes to the increase of the electron density, not the electron temperature. The high electron density can facilitate the dissociation of  $\text{SiH}_4$ ,  $\text{PH}_3$ , and  $\text{H}_2$ , and thus accelerate the deposition rate, as shown in Figure 9.



(a)



(b)

**Figure 8.** Power effects on (a) radicals intensities and (b) radicals intensities ratio.

$SiH_4/H_2/PH_3$  (6.88% in  $H_2$ ) 35/1000/20 sccm, 800 mT, and 250°C.

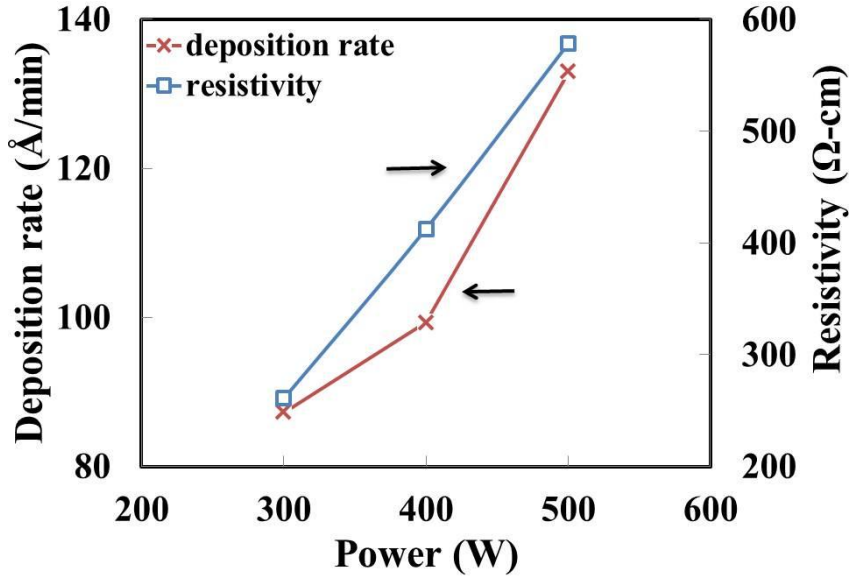


**Figure 9.** Power effect on the deposition rate and resistivity.  $\text{SiH}_4/\text{H}_2/\text{PH}_3$  (6.88% in  $\text{H}_2$ ) 35/1000/20 sccm, 800 mT, and 250°C.

In addition, the film resistivity increases with the increase of power. In the steady-state plasma, deposition precursors such as  $\text{SiH}_3$ ,  $\text{SiH}_2$ , and  $\text{SiH}$  are produced by inelastic collision of higher energy electron with  $\text{SiH}_4$ . Since  $\text{SiH}_3$  has only one active point and is not easy to react with other species, it is the dominant precursor for film deposition. Highly reactive species such as  $\text{SiH}_2^*$  and  $\text{SiH}^*$  are also produced simultaneously in the plasma. For example,  $\text{SiH}_2$  is given by



$\text{SiH}_3$  has larger amount in the plasma than  $\text{SiH}_2$  does due to the lower dissociation threshold energy. Also, there are more ways to produce  $\text{SiH}_3$  [34]. For example,  $\text{SiH}_3$

can be produced not only by collision of SiH<sub>4</sub> with higher energy e<sup>-</sup> but also by H+SiH<sub>4</sub> (abstraction reaction), which is given by



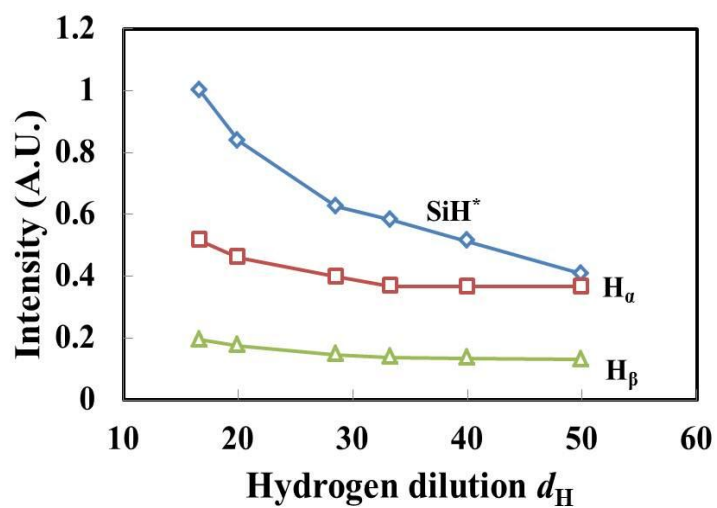
Since SiH<sub>2</sub> production needs higher threshold energy, higher power results in the increase of SiH<sub>2</sub>. Another reason is as followed: in this experiment, SiH<sub>4</sub> is feeding with 35 sccm of flow rate. When high electric power is applied to the plasma under such a low SiH<sub>4</sub>-flow-rate condition, SiH<sub>4</sub> is highly dissociated followed by depletion. The gas-phase-reaction probabilities of short lifetime species with SiH<sub>4</sub> is reduced, leading to an increase of contribution ratio of short life time species, such as SiH<sub>2</sub><sup>\*</sup>, to the film growth at high plasma power [7]. M. Kumeda *et al.* reported that the deterioration of the film is due to the increase of SiH<sub>2</sub> type bonding and the decrease of SiH type bonding. It is because the formation of SiH<sub>2</sub> type bonding increases the defect density in contrast with SiH type bonding which serves to decrease the defect density [35]. T. Nishimoto *et al.*

also reported that the short lifetime radical such as  $\text{SiH}_2^*$  generate higher-order-silane related species such as  $\text{Si}_2\text{H}_6$  and  $\text{Si}_3\text{H}_8$ . Those higher-order-silane species increases the amount of dangling-bond and microvoid in the film, leading to the deterioration of film quality [37]. It is likely that  $(\text{SiH}_2)_n$  raises the possibility for the origin of voids, and  $\text{SiH}$  is simply a dangling-bond terminator [36]. The amount of weak Si-Si bonds is proportional to the ratio of  $\text{SiH}_2/\text{SiH}$ . Also, the increase of ion bombardment (high power density) gives rise to the increase of defect density. Therefore, the increase of  $\text{H}_\alpha^*/\text{SiH}^*$  with the rise of power indicates less formation of  $\text{SiH}$  and more formation of  $\text{SiH}_2$ , leading to the deterioration of film quality with higher resistivity. However, it's not necessary the lower power the better. Moderated ion bombardment and dangling bond passivation by atomic hydrogen are needed to get a good quality film. In this experiment, the lowest resistivity  $n^+$  film by varying plasma power is 260.92 ( $\Omega\text{-cm}$ ). It was deposited at 35 sccm  $\text{SiH}_4$ , 1000 sccm  $\text{H}_2$ , 20 sccm  $\text{PH}_3$  (6.88% in  $\text{H}_2$ ), 800 mT, 300 W, and 250°C.

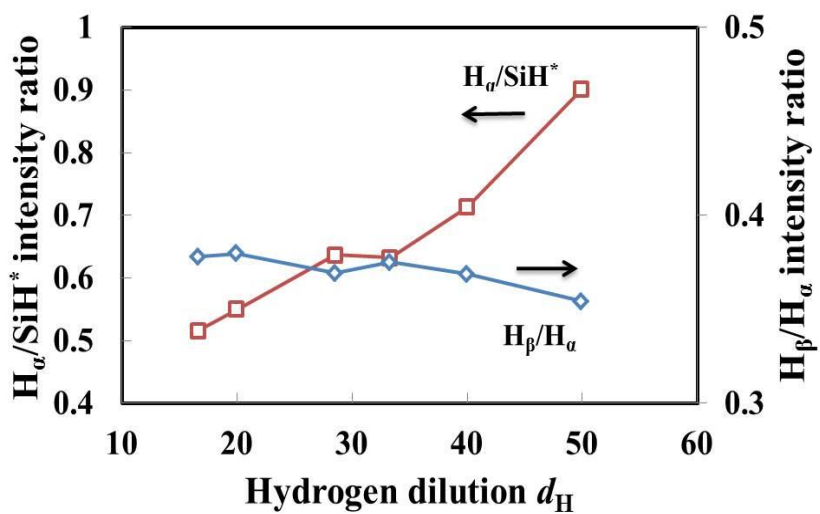


### 3.4.2 Hydrogen Dilution Effect

Figure 10 shows the hydrogen dilution ( $d_{H=H_2/f_{SiH_4}}$ ) effect on the radicals intensities by varying the  $SiH_4$  flow rate. The gas flow rate is  $SiH_4/H_2/PH_3$  (6.88% in  $H_2$ ) 20-60/1000/20 sccm, 300 W, 800 mT, 250°C. The hydrogen dilution varied in the range of 17-50 in this experiment. The  $SiH^*$  intensity decreases monotonically with the decrease of  $SiH_4$  flow rate. The intensities of  $H_\alpha$  and  $H_\beta$  decrease a little and are constant in general due to the decrease of  $SiH_4$ -dissociation-produced  $H_2$ . The  $H_\alpha/SiH^*$  ratio increases with hydrogen dilution, reflecting the increasing concentration of atomic hydrogen. It is reported that the  $H_\alpha/SiH^*$  ratio could be related to the crystallinity in the film [24]. Above a certain value of  $H_\alpha/SiH^*$  ratio, the amount of atomic hydrogen is enough to induce nucleation. All the  $n^+$  films in Figure 10 are amorphous as confirmed with the Raman spectroscopy, i.e., only a broad feature near  $480\text{ cm}^{-1}$ . Also, the hydrogen dilution has almost no influence on the  $T_e(H_\beta/H_\alpha)$ .  $T_e$  is mainly affected by the power and pressure, typically increases with the increase of power and with the decrease of pressure [37]. Since the power and pressure are constant, the  $T_e$  didn't change a lot.



(a)



(b)

**Figure 10.** Hydrogen dilution effect on (a) radicals intensities, and (b) radicals intensities ratio.  $\text{SiH}_4/\text{H}_2/\text{PH}_3$  (6.88% in  $\text{H}_2$ ) 20-60/1000/20 sccm, 800 mT, 300 W, and 250°C.

Figure 11 shows that the deposition rate decreases with the increase of hydrogen dilution. This can be attributed to two reasons. (1) The decrease of  $\text{SiH}_4$  precursor's concentration, leading to the decrease of dissociation rate (forward reaction in equation 3.7). (2) The atomic hydrogen can etch weak Si-Si bonds to form strong Si-Si bonds. With the increasing hydrogen dilution, the etching rate of the atomic hydrogen increases and retards the deposition rate (reverse reaction in equation 3.7). The presence of hydrogen in amorphous silicon is known to be necessary for the achievement of high quality amorphous silicon by saturating dangling bonds and decrease density of gap state [38]. In unhydrogenated a-Si, the Fermi energy cannot be moved by doping due to large density of defects [39]. The moderate amount of hydrogen incorporation into amorphous silicon is essential during doping. However, heavy hydrogen dilution gives depletion effects on  $\text{SiH}_4$ . Mark J. Kushner has reported that the  $\text{SiH}_3$  production rate by electron impact dissociation is maximum near the electrodes, whereas that by hydrogen abstraction is maximum in the bulk [40]. With the heavy hydrogen dilution,  $\text{SiH}_4$  is quickly consumed by hydrogen abstraction reaction. Donker *et al.* also reported that the high hydrogen dilution suppressed the  $\text{SiH}_4$  back diffusion from the reaction chamber into the process zone due to its transient depletion [41]. As the  $\text{SiH}_4$  highly depleted, short-lifetime species such as  $\text{SiH}_2$  near the electrode contributed dominantly on the film growth. The short-lifetime species stacked with high reactivity on the growing film surface without surface diffusion to form Si-Si bonds after insertion into Si-H bonds. Under this circumstance, the density of dangling-bond defects in the films increases [42]. Therefore, the resistivity increases with the increase of the  $\text{H}_\alpha^*/\text{SiH}^*$  ratio due to the

increase of the  $H_u^*$  intensity and the decrease of the  $SiH^*$  intensity. The lowest resistivity  $n^+$  film by varying  $SiH_4$  flow rate is 94.23 ( $\Omega\text{-cm}$ ). It was deposited at 60 sccm  $SiH_4$ , 1000 sccm  $H_2$ , 20 sccm  $PH_3$  (6.88% in  $H_2$ ), 800 mT, 300 W, and 250°C.

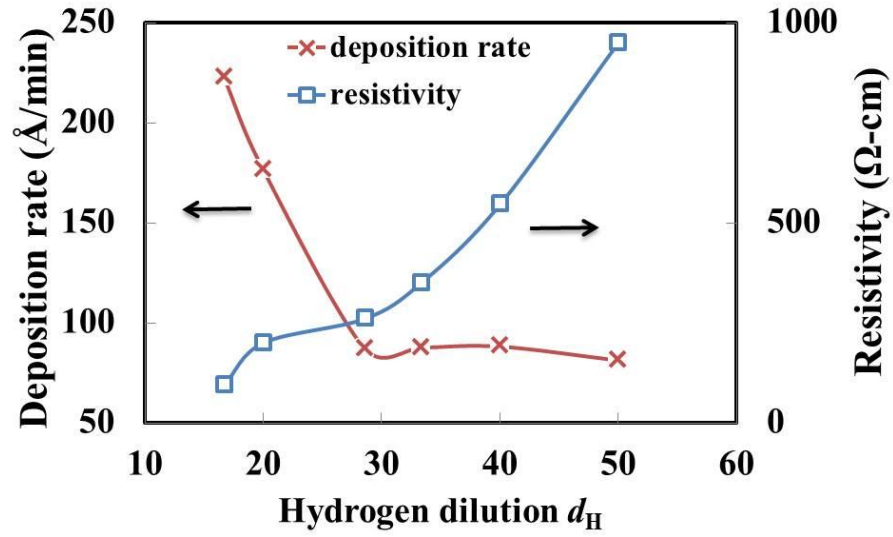


**Figure 11.** Hydrogen dilution effect on the deposition rate and resistivity.  $SiH_4/H_2/PH_3$  (6.88% in  $H_2$ ) 20-60/1000/20 sccm, 300 W, 800 mT, and 250°C.

### 3.4.3 Pressure Effect

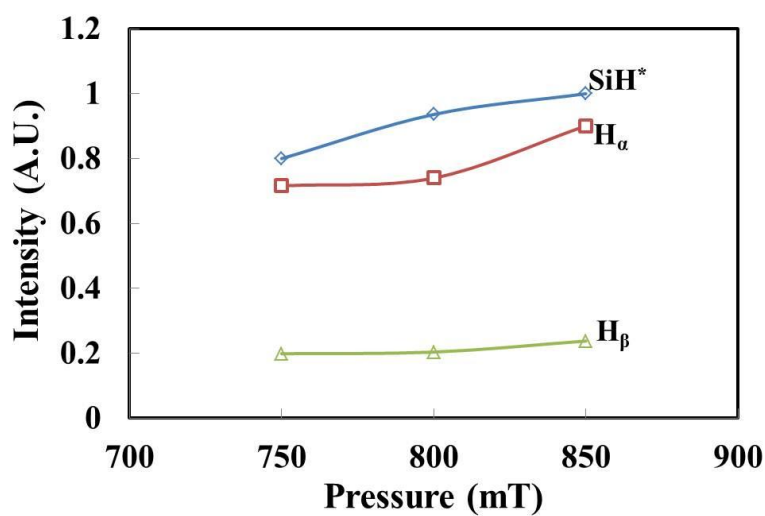
Figure 12(a) shows the pressure effect on the radicals intensities at  $\text{SiH}_4/\text{H}_2/\text{PH}_3=60/1000/20$  sccm, 300 W, 250°C. It is observed that increasing pressure cause the increase of  $\text{SiH}^*$ ,  $\text{H}_\alpha$ , and  $\text{H}_\beta$ . Plasma modeling showed that with increasing pressure, the partial pressure of  $\text{SiH}_4$  and  $\text{H}_2$  increase, and the mean free path of gas atom becomes shorter [32]. The relation of total gas pressure and the mean free path is given by

$$\lambda = \frac{kT}{\sqrt{2}\pi d^2 p} \quad (3.10)$$

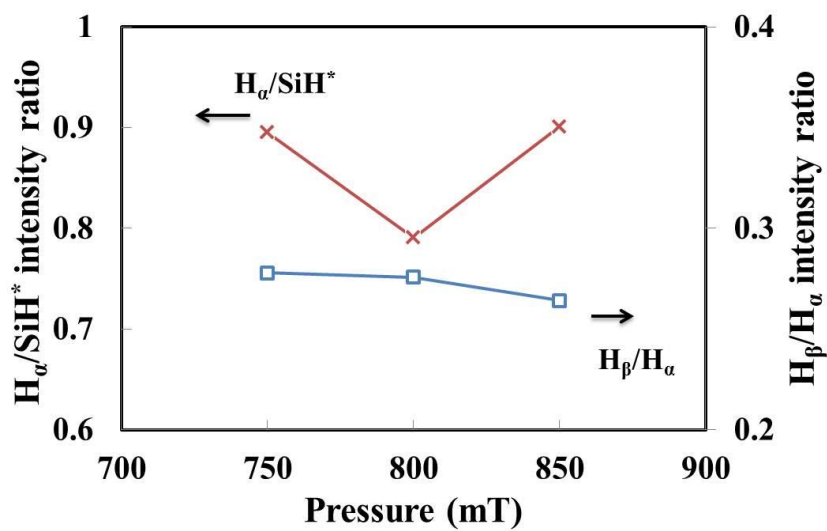
where  $\lambda$  is the mean free path,  $P$  is the gas pressure,  $k$  is Boltzmann's constant,  $T$  is the temperature, and  $d$  is the diameter of a molecule. The electron density distribution shifts to lower energy due to the increasing possibility of collisions, resulting in a reduction of the electron density  $N_e$  with the energy above the threshold value. The increase of  $[\text{SiH}_4]$  and the decrease of  $N_e$  compete each other in determining  $I(\text{SiH}^*)$ . Thus, a balance between the increase in dissociation rate due to increase  $\text{SiH}_4$  partial pressure and decrease of dissociation due to reduced electron temperature limits the maximum of  $I(\text{SiH}^*)$ . Similarly, the atomic hydrogen concentration increase with the rise of pressure. However, the loss of the atomic hydrogen due to abstraction reaction also becomes significant due to high reactant concentration. Also, since the energy temperature is reduced, the dissociation rate is retard in high pressure condition. The atomic hydrogen in the gas phase was calculated by the creation rate of atomic hydrogen and the loss rate of abstraction reactions in the gas phase.

Figure 12(b) shows the pressure effect on the radical intensities ratio. The  $H_\beta/H_\alpha$  ratio decreases a little which indicates the reduced electron temperature due to the increasing number of collisions. The  $H_\alpha/\text{SiH}^*$  ratio has a minimum at 800 mT, which is determined by the balance of creation rate and loss rate of  $\text{SiH}^*$  and  $H_\alpha$ . Plasma modeling shows that for the PECVD which featured with shower head gas inlet and operated in over 100 W, the creation rate is substantially higher compared to the hydrogen loss due to abstraction [32]. However, if the  $\text{SiH}_4$  concentration is high, the decrease of the atomic hydrogen concentration due to abstraction becomes significant. The increase of  $I(\text{SiH}^*)$  due to the  $\text{SiH}_4$  depletion and the decrease of  $I(H_\alpha^*)$  due to abstraction reaction leads to the decrease of  $H_\alpha/\text{SiH}^*$  ratio in high pressure. Based on this complicated mutual reaction, the dependence of  $H_\alpha/\text{SiH}^*$  ratio on pressure should not have a single trend in this case.

Figure 13 shows the pressure effect on the deposition rate and resistivity. The deposition rate is determined by a balance between the increase of dissociation rate due to increased  $\text{SiH}_4$  partial pressure and the decrease of dissociation rate due to decreased electron temperature. The maximum deposition rate is at the 850 mT in which the  $\text{SiH}^*$  has the highest intensity. The film resistivity shows a minimum at 800 mT, which has a similar trend as  $H_\alpha/\text{SiH}^*$  ratio, which can be explained by the highly hydrogen abstraction induced  $\text{SiH}_4$  depletion as previously mentioned. The lowest resistivity  $n+$  film by varying pressure is 94.23 ( $\Omega\text{-cm}$ ). It was deposited at 60 sccm  $\text{SiH}_4$ , 1000 sccm  $\text{H}_2$ , 20 sccm  $\text{PH}_3$  (6.88% in  $\text{H}_2$ ), 800 m, 300 W, and 250°C.



(a)



(b)

**Figure 12.** Pressure effect on (a) radicals intensities, and (b) radicals intensities ratio.

SiH<sub>4</sub>/H<sub>2</sub>/PH<sub>3</sub> (6.88% in H<sub>2</sub>) 60/1000/20 sccm, 300 W, and 250°C.

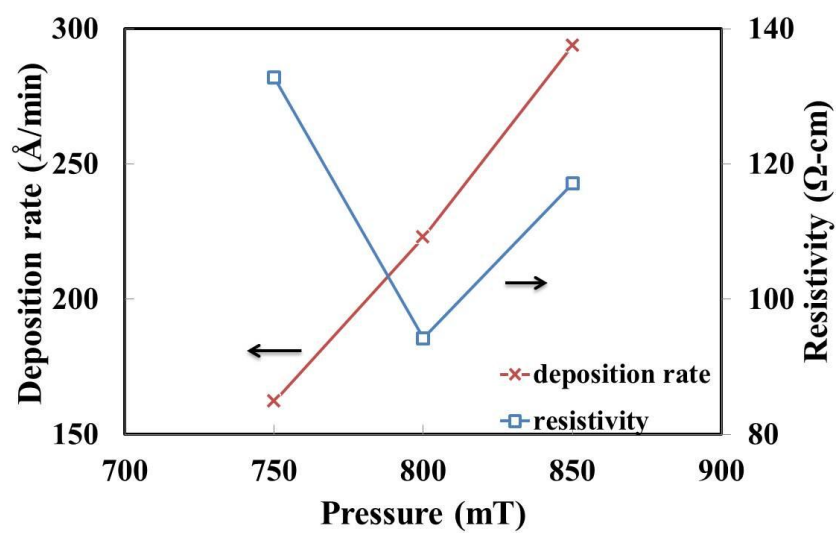


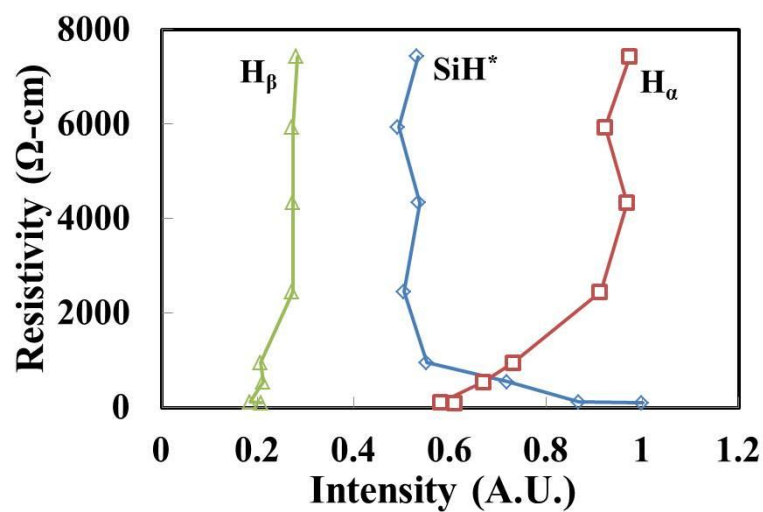
**Figure 13.** Pressure effect on the deposition rate and resistivity.  $\text{SiH}_4/\text{H}_2/\text{PH}_3$  (6.88% in  $\text{H}_2$ ) 60/1000/20 sccm, 300 W, and 250°C.



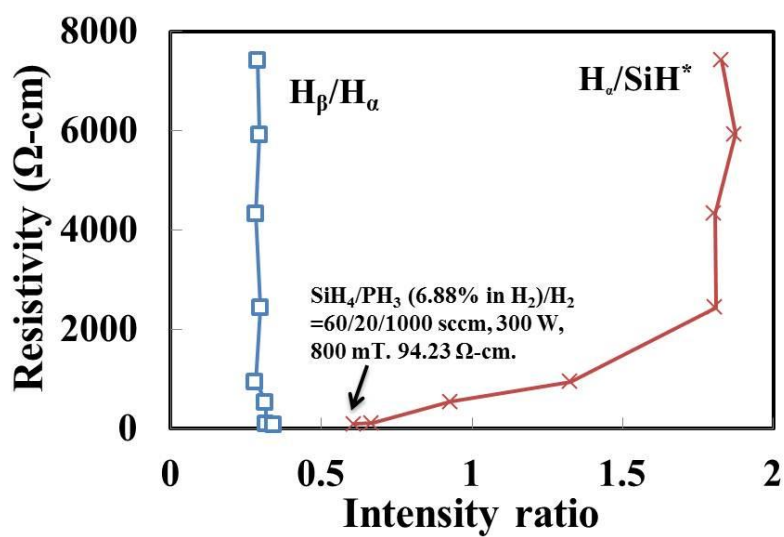
#### 3.4.4 The Relationship Between $H_\alpha/SiH^*$ and $n^+$ Film Resistivity

Figure 14(a) shows the radicals concentrations vs. the  $n^+$  film resistivity. The samples were prepared under different process conditions, e.g., flow rates of  $SiH_4$  (10-60 sccm),  $PH_3$  (6.88% in  $H_2$ ) (1-20 sccm), and  $H_2$  (1000 sccm), power (300-500 W), and pressure (750-850 mT). The hydrogen dilution ( $d_H$ ) is in the range of 17 to 100. The  $n^+$  resistivity is determined by (1) the concentration of electrically active dopants, and (2) the morphology. The  $n^+$  films produced in this experiment are all a-Si:H, i.e. the morphology of these films are similar. The resistivity increases with the increase of the  $H_\alpha^*$  intensity but decreases with the increase of the  $SiH^*$  intensity. Also, the resistivity increases drastically with the slight increase of the  $H_\beta^*$  intensity but smoothly with the increase of the  $H_\alpha^*$  intensity. According to Spear and Le Comber, when the  $PH_3/SiH_4$  ratio in the feed stream is higher than 0.01, the P incorporation saturates at  $10^{-3}$  in the film, e.g.  $5 \times 10^{-19} \text{ cm}^{-3}$  [43]. The range of  $PH_3/SiH_4$  ratio in Figure 14 is 0.014-0.023. Therefore, at the low  $SiH^*$  and high  $H_\alpha^*$  intensity conditions, which corresponds to the low  $SiH_4$  and high  $H_2$  dissociation efficiencies, P atoms are probably incorporated in the electrically inactive form, rather than substitutionally located in the film [44]. Also, the higher dissociation rate of  $H_2$  can lead to higher possibility to form  $PH_x$  in the film, which does not contribute to the conductivity. H atoms can passivate the dangling bond to increase the carrier lifetime, but it can also lead to the coexistence of  $SiH$ ,  $SiH_2$  and  $SiH_3$  in the film, which lowers the charge carrying capability [17]. Therefore, the resistivity increases with the increase of the  $H_\alpha^*/SiH^*$  ratio due to the increase of the  $H_\alpha^*$  intensity and the decrease of the  $SiH^*$  intensity.

Figure 14(b) shows that when the  $H_{\alpha}^*/SiH^*$  ratio is increased from 0.6 to 1.8, the resistivity increases almost 100 times. As previously mentioned, the formation of  $SiH_2$  type bonding increases the defect density in contrast with  $SiH$  type bonding which serves to decrease the defect density. The amount of weak Si-Si bonds is proportional to the ratio of  $SiH_2/SiH$ . Therefore, the increase of  $H_{\alpha}^*/SiH^*$  indicates less formation of  $SiH$  and more formation of  $SiH_2$  due to too much hydrogen in the plasma, leading to the deterioration of film quality with higher resistivity. However, it's not necessary the lower  $H_{\alpha}^*/SiH^*$  ratio the better. Moderated ion bombardment and dangling bond passivation by atomic hydrogen are needed to get a good quality film. This statement is valid in a specific hydrogen dilution range and  $H_{\alpha}^*/SiH^*$  ratio range for only doped silicon film, i.e. the condition which has doping gas in the feeding stream. For example, for the *i*- layer deposited at  $SiH_4$  50 sccm, 100 W, and 500 mT, the  $H_{\alpha}^*/SiH^*$  ratio is very low, about 0.015. However, the resistivity is too high for the 4-point probe measurement due to the low dopant concentration. It also shows that the film's resistivity is almost not affected by the  $H_{\beta}^*/H_{\alpha}^*$  ratio, i.e., the  $T_e$ . Generally, the  $H_{\alpha}^*/SiH^*$  ratio could be affected



(a)



(b)

**Figure 14.**  $n^+$  film resistivity vs. (a)  $SiH^*$ ,  $H_\alpha^*$ , and  $H_\beta^*$  intensities, and (b)  $H_\alpha^*/SiH^*$  and  $H_\beta^*/H_\alpha^*$  ratios.

by power, pressure, and feeding gas flow rate. For example, the higher power can increase the dissociation of feeding gases, and change the ratio. Both SiH<sub>4</sub> and PH<sub>3</sub> (2%) can produce the signal of H radicals, e.g. dissociation of SiH<sub>4</sub> can produce H radicals, and the PH<sub>3</sub> (2%) contains 98% H<sub>2</sub>.

The relationship between resistivity and  $H_{\alpha}^*/SiH^*$  ratio can be confirmed by Figure 10 and Figure 11 with varying hydrogen dilution, or by Figure 12 and Figure 13 with varying pressure. For example, with the increasing power in the same PH<sub>3</sub> flow rate, the resistivity decreases with the reduction of the  $H_{\alpha}^*/SiH^*$  ratio because the SiH<sup>\*</sup> intensity increases faster than the  $H_{\alpha}^*$  intensity does, leading to more electrically activated P dopants in the film, as shown in Figure 12 and Figure 13. Therefore, the low  $n^+$  film resistivity can be obtained by adjusting the deposition parameters, such as power, pressure, and feed gas composition, toward the low  $H_{\alpha}^*/SiH^*$  ratio [45]. For example, within the deposition conditions in this study, the lowest resistivity of 94.23  $\Omega$ -cm was obtained under the condition of SiH<sub>4</sub>/PH<sub>3</sub> (6.88% in H<sub>2</sub>)/H<sub>2</sub> 60/20/1000 sccm, 300 W, 800 mT, and 250°C.

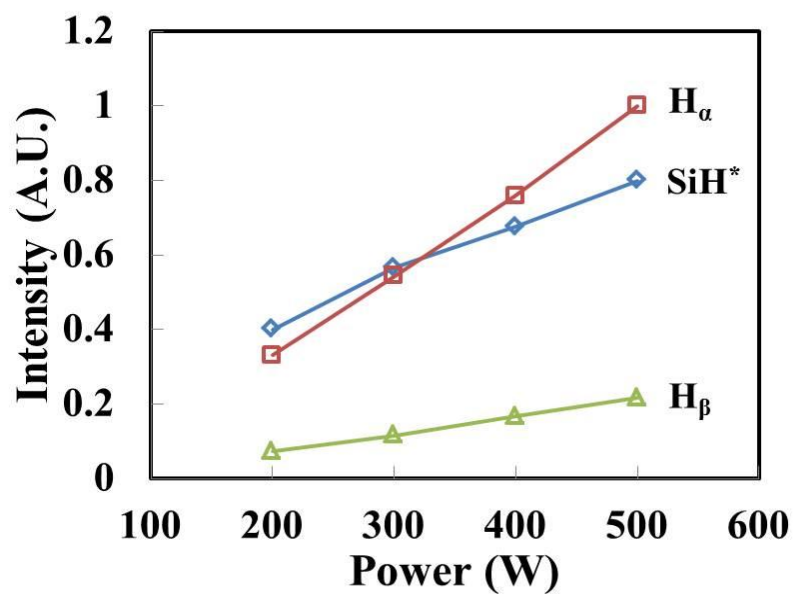
### 3.5 Emission Spectra of $p^+$ a-Si:H Film Deposition

#### 3.5.1 Power Effect

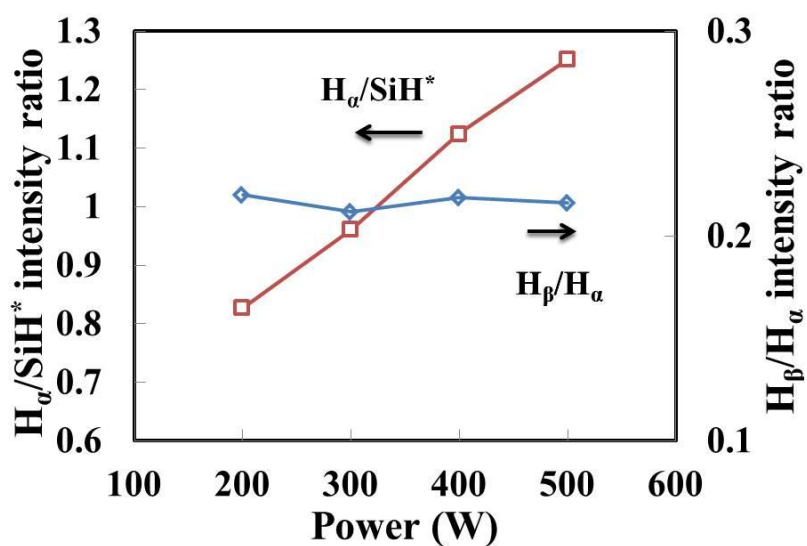
In the  $p^+$  a-Si:H deposition processes, the optical emission from the BH (433 nm), and B line (250 nm) could not be detected probably due to the low dopant gas concentration in the feed gas stream, e.g., 0.15%-0.37% for  $B_2H_6$ . The  $SiH^*$ ,  $H_\alpha^*$ ,  $H_\beta^*$ , and  $H_2$  concentrations in the  $SiH_4/H_2/B_2H_6$  plasmas are almost the same as those in the  $SiH_4/H_2$  plasma. For the  $p^+$  film deposition, the feed stream was composed of  $SiH_4$  (10-35 sccm),  $H_2$  (400-1000 sccm), and  $B_2H_6$  (2% in  $H_2$ ) (10-100 sccm). The hydrogen dilution ( $d_H$ ) is in the range of 14 to 100. Since it is similar to the hydrogen dilution range of  $n^+$  deposition ( $d_H=17-100$ ), the deposition parameter effect on  $p^+$  deposition should be generally similar to that on  $n^+$  except the small range of  $d_H=14-17$ . Figure 15(a) shows the power effect on the radical intensities at  $SiH_4/H_2/B_2H_6$  (2% in  $H_2$ ) 35/400/100 sccm, 800 mT, 250°C. The  $d_H$  is 14.22, which is in that small exception range. All intensities increase with the increase of power. For example, the  $SiH^*$  and  $H_\alpha^*$  intensities at 500 W are 2 and 3 times those at 200W, separately. The increase of the  $H_\alpha^*$  intensity is more obvious than the increase of the  $SiH^*$  intensity. Figure 15(b) shows that the  $H_\alpha^*/SiH^*$  ratio increases with the increase of power. It is because that  $H_2$  can be contributed by the dissociated  $SiH_4$  and the feed gas, but  $SiH^*$  can only be from of the

dissociated  $\text{SiH}_4$ . The electron temperature is not influenced by the increase of power since  $H_\beta^*/H_\alpha^*$  ratio is almost constant. Therefore, in this case the increase of the power mainly contributes to the increase of the electron density, not the electron temperature. The high electron density can facilitate the dissociation of  $\text{SiH}_4$ ,  $\text{B}_2\text{H}_6$ , and  $\text{H}_2$ , and thus accelerate the deposition rate, as shown in Figure 16.

Different from the result of  $n^+$ , the film resistivity decreases with the increase of  $H_\alpha^*/\text{SiH}^*$  ratio. It is probably because the reactant gas is feeding with a moderate hydrogen dilution ( $d_{\text{H}}=14$ ). The atomic hydrogen can passivate the dangling bonds and etch weak Si-Si bond by ion bombardment, and enhance the electrical properties of the film [29, 30]. In addition, the moderate increase of abstraction reaction by reaction of  $\text{SiH}_4$  with H without depleting  $\text{SiH}_4$  can increase the  $\text{SiH}_3$  concentration and reduce the  $\text{SiH}_2$  concentration, leading to a dense silicon network in the film. In this experiment, the lowest resistivity  $n^+$  film by varying plasma power is 202.51 ( $\Omega\text{-cm}$ ). It was deposited at 35 sccm  $\text{SiH}_4$ , 400 sccm  $\text{H}_2$ , 100 sccm  $\text{B}_2\text{H}_6$  (2% in  $\text{H}_2$ ), 450 mT, 500 W, and 250°C.



(a)



(b)

**Figure 15.** Power effects on (a) radicals intensities and (b) radicals intensities ratio.

$SiH_4/H_2/B_2H_6$  (2% in  $H_2$ ) 35/400/100 sccm, 800 mT, and 250°C.

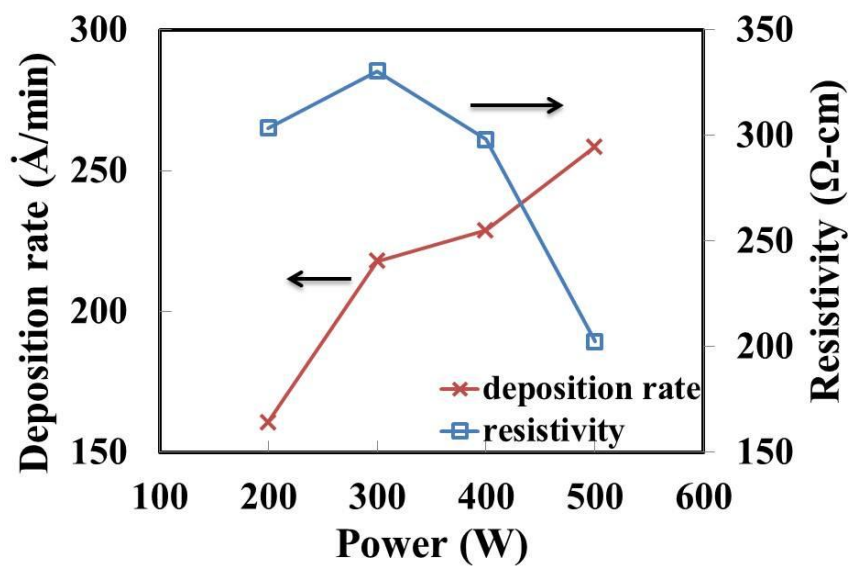
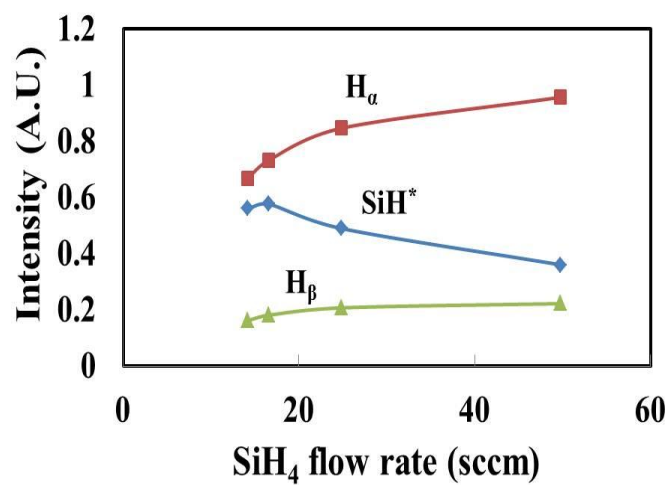


**Figure 16.** Power effect on the deposition rate and resistivity.  $\text{SiH}_4/\text{H}_2/\text{B}_2\text{H}_6$  (2% in  $\text{H}_2$ )  
35/400/100 sccm, 800 mT, and 250°C.

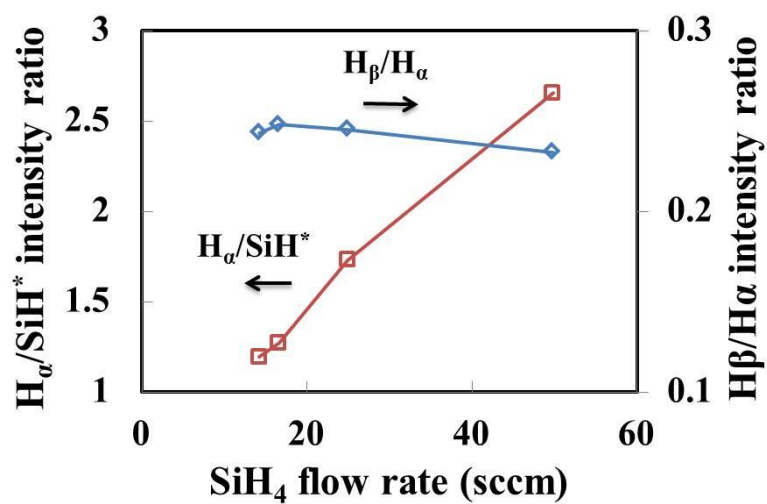


### 3.5.2 Hydrogen Dilution Effect

Figure 17 shows the hydrogen dilution ( $d_H=f_{H_2}/f_{SiH_4}$ ) effect on the radicals intensities by varying the  $SiH_4$  flow rate. The gas flow rate is  $SiH_4/H_2/B_2H_6$  (2% in  $H_2$ ) 10-35/400/100 sccm, 500W, 450 mT, 250°C. The hydrogen dilution varied in the range of 14-50 in this experiment. The  $SiH^*$  intensity decreases monotonically with the decrease of  $SiH_4$  flow rate. The intensities of  $H_\alpha$  and  $H_\beta$  increase due to the increase of  $H_2$  ratio. The  $H_\alpha/SiH^*$  ratio increases with hydrogen dilution, reflecting the increasing concentration of atomic hydrogen. The hydrogen dilution has almost no influence on the  $T_e$  ( $H_\beta/H_\alpha$ ).  $T_e$  is mainly affected by the power and pressure, typically increases with the rise of power and with the reduction of pressure [37]. Since the power and pressure in are constant, the  $T_e$  didn't change a lot. Figure 18 shows that the deposition rate decreases with the increase of hydrogen dilution. This can be attributed to the decrease of  $SiH_4$  precursor's concentration and the increase of hydrogen dilution, which leads to the decrease of dissociation rate and the increase of etch rate, respectively. In addition, the resistivity increases with the increase of the  $H_\alpha^*/SiH^*$  ratio. The resistivity seems to be inversely proportional to the deposition rate in this case. . The deterioration of the film stability accompanied by an increase of deposition rate was found to be closely correlated with the increase of Si- $H_2$  bond hydrogen content in the deposited film [35]. As previously mentioned, heavy hydrogen dilution gives depletion effects on  $SiH_4$ . Short-lifetime species such as  $SiH_2$ ,  $SiH$ , and  $Si$  near the electrode contributed dominantly on the film growth, giving rise to the increase of the density of dangling-



(a)



(b)

**Figure 17.** Hydrogen dilution effect on (a) radicals intensities, and (b) radicals intensities ratio. SiH<sub>4</sub>/H<sub>2</sub>/B<sub>2</sub>H<sub>6</sub> (2% in H<sub>2</sub>) 10-35/400/100 sccm, 450 mT, 500 W, and 250°C.

bond defects in the films. The lowest resistivity  $n^+$  film by varying  $\text{SiH}_4$  flow rate is 202.51 ( $\Omega\text{-cm}$ ). It was deposited at 35 sccm  $\text{SiH}_4$ , 400 sccm  $\text{H}_2$ , 100 sccm  $\text{B}_2\text{H}_6$  (2% in  $\text{H}_2$ ), 450 mT, 500 W, and 250°C.

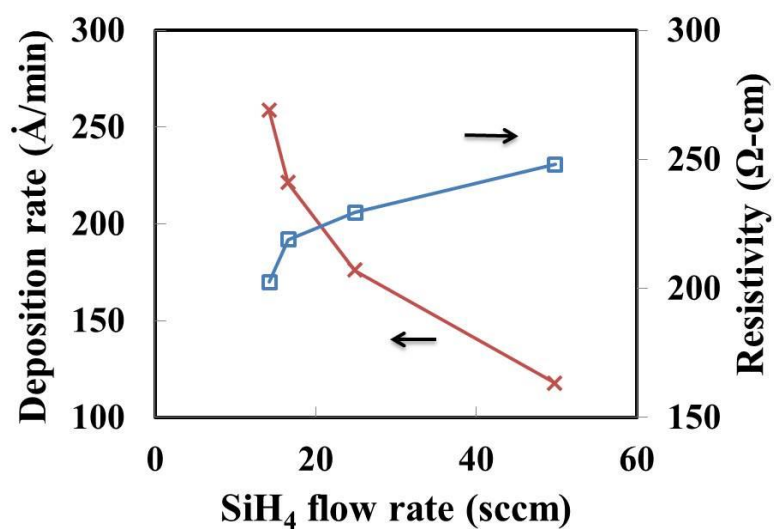
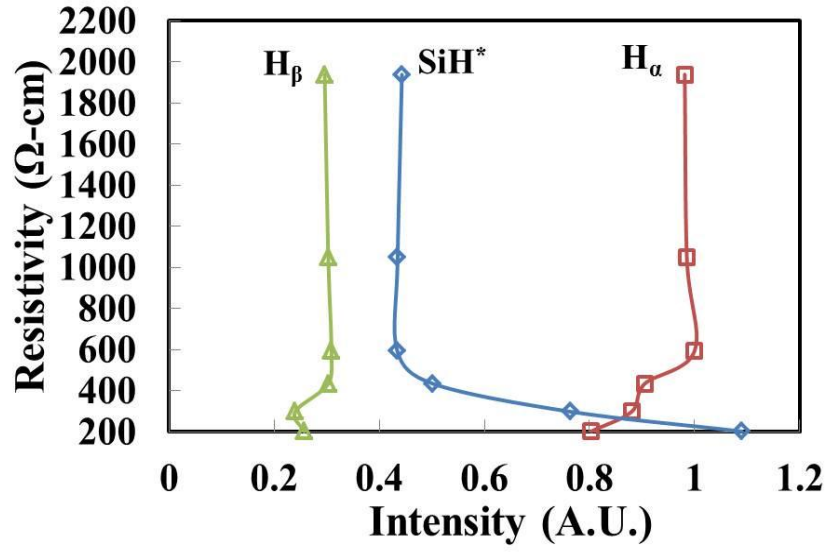


**Figure 18.** Hydrogen dilution effect on the deposition rate and resistivity.  $\text{SiH}_4/\text{H}_2/\text{B}_2\text{H}_6$  (2% in  $\text{H}_2$ ) 10-35/400/100 sccm, 450 mT, 500 W, and 250°C.

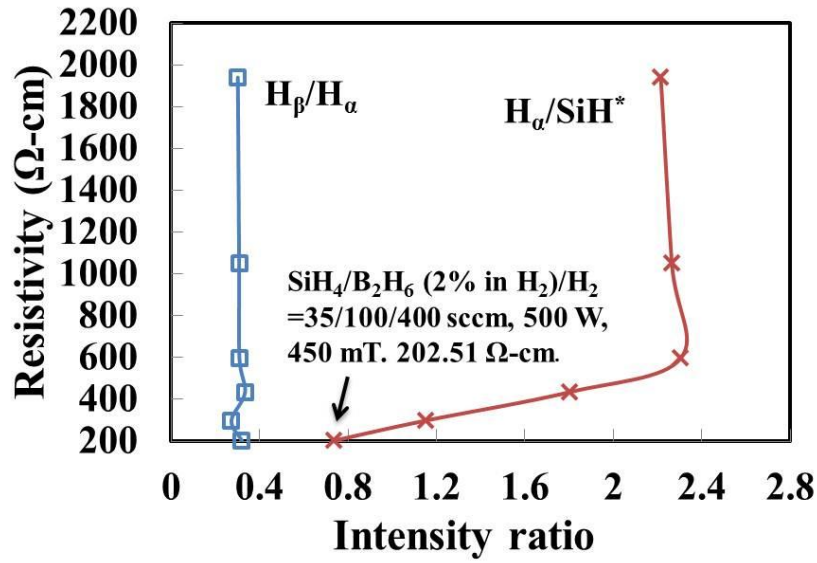
### 3.5.3 The Relationship between $H_\alpha^*/SiH^*$ and $p^+$ Film Resistivity

Figure 19(a) shows the radicals concentrations vs. the  $p^+$  film resistivity. The samples were prepared under different process conditions, e.g., flow rates of  $SiH_4$  (10-35 sccm),  $B_2H_6$  (2% in  $H_2$ ) (10-100 sccm), and  $H_2$  (400-1000 sccm), power (400-500 W), and pressure (450-750 mT). The hydrogen dilution ( $d_H$ ) is in the range of 14 to 100. The  $n^+$  resistivity is determined by (1) the concentration of electrically active dopants, and (2) the morphology. The  $n^+$  films produced in this experiment are all a-Si:H, i.e. the morphology of these films are similar. The resistivity increases with the increase of the  $H_\alpha^*$  intensity but decreases with the increase of the  $SiH^*$  intensity. The  $H_\beta^*$  intensity does not affect the resistivity so much. Figure 14(b) shows that when the  $H_\alpha^*/SiH^*$  ratio is increased from 0.7 to 2.3, the resistivity increases almost 10 times. It also shows that the film's resistivity is almost not affected by the  $H_\beta^*/H_\alpha^*$  ratio, i.e., the  $T_e$ .

The relationship between  $p^+$  resistivity and  $H_\alpha^*/SiH^*$  ratio can be confirmed by Figure 17 and Figure 18 with varying hydrogen dilution in the same range. However, with small hydrogen dilution, e.g.  $d_H=14$ , the opposite trend is observed, which can be confirmed by Figure 15 and Figure 16. It reveals that the hydrogen dilution is critical in the plasma. Moderate hydrogen dilution is helpful for dangling bonds passivation and weak Si-Si bond etching. However, heavy hydrogen dilution leads to the  $SiH_4$  depletion and increase the  $SiH_2$  concentration, which can deteriorate the film electrical properties and stability. The  $H_\alpha^*/SiH^*$  ratio can be affected by the deposition parameters such as power, pressure, and gas flow rate. Therefore, the low  $p^+$  film resistivity can be obtained by adjusting toward the moderate  $H_\alpha^*/SiH^*$  ratio. For example, within the deposition



(a)



(b)

**Figure 19.**  $p^+$  film resistivity vs. (a)  $SiH^*$ ,  $H_\alpha^*$ , and  $H_\beta^*$  intensities, and (b)  $H_\alpha^*/SiH^*$  and  $H_\beta^*/H_\alpha^*$  ratios.

conditions in this study, the lowest resistivity of 202.51  $\Omega$ -cm was obtained under the condition of  $\text{SiH}_4/\text{B}_2\text{H}_6$  (2% in  $\text{H}_2$ )/ $\text{H}_2$  35/100/400 sccm, 500 W, 450 mT.

CHAPTER IV  
PIN DIODE WITH AMORPHOUS SILICON UNDER SOLAR LIGHT  
ILLUMINATION

#### 4.1 Introduction

This chapter investigated the performance of the PIN diode with amorphous silicon under solar light illumination. The factors which influence the efficiency are also studied.

#### 4.2 Experimental Method

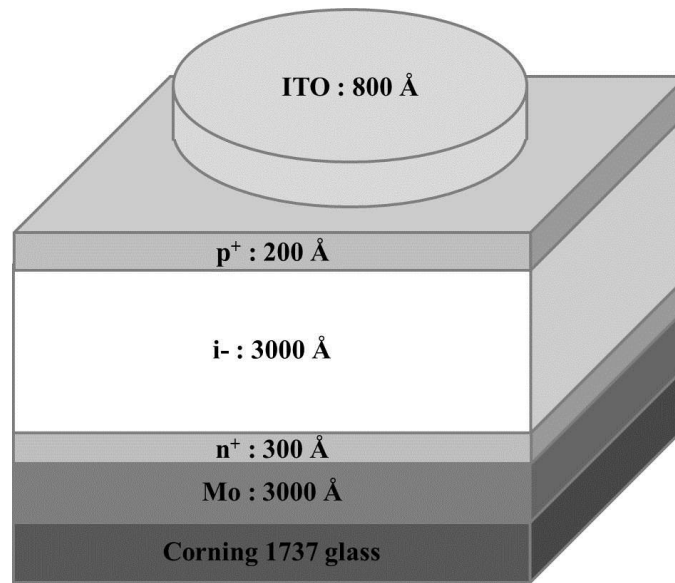
The a-Si:H PIN stacks was deposited by a plasma enhanced chemical vapor deposition (PECVD) system, which has the parallel-plate electrode arrangement driven by a 13.56 MHz RF generator. The  $n^+$ ,  $i$ -,  $p^+$  film was deposited on the corning 1737 glass substrate pre-coated with a sputter deposited Mo (3000 Å ) film. After each layer was deposited, the chamber was purge with a series of high- and low-pressure argon streams to remove the residue gas. These a-Si:H thin films were deposited sequentially in one-pump down in the same chamber without breaking the vacuum. An indium tin oxide (ITO) film was sputtered at a rate of 2 nm/min from pure Ar, 80 W, 5 mT on top of the PIN stack. This ITO film was then patterned into the round electrodes (2 mm, 3 mm, 4 mm, 5 mm, 8 mm, and 11 mm in diameter) by photolithography and etched with HCl/HNO<sub>3</sub> (3/1) solution. The finished PIN diode was annealed in atmosphere at 200°C

for 30 min to repair the plasma damage introduced during sputter. Figure 20 shows the cross-section view and top view of the diode.

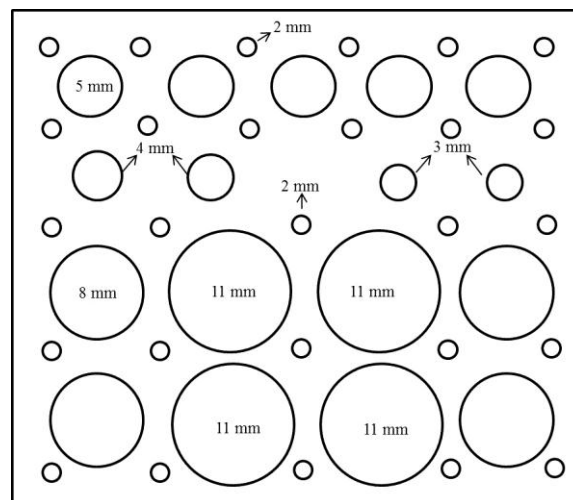
The current density-voltage ( $J$ - $V$ ) curves of the diode were measured in the dark, under the solar light illumination, and under mono-wavelength light illumination. The solar light was produced by solar light simulator 16S-300-002 from Solar Light Co., Inc. The power density of the solar light was fixed at 1000 W/m<sup>2</sup>. The mono-wavelength light was introduced by using different LEDs, M625L2, M530L2 and M470L2 from Thorlabs, i.e., red at 625 nm, green at 530 nm, and blue at 470 nm. The photon energies of the red, green, and blue LEDs are 1.98 eV, 2.34 eV, and 2.64 eV separately which are larger than the band gap energy of a-Si:H i.e., 1.7 eV. The power density of the LED was fixed at 28.4 W/m<sup>2</sup>.

The  $J$ - $V$  measurements were carried out using the Agilent 4140B parameter analyzer in a sweep mode with increment of 0.01 V. The gate voltage  $V_g$  was swept from -3 V to 3 V for the  $J$ - $V$ . All measurements were made in the probe station in a black box.





(a)



(b)

**Figure 20.** (a) Cross-section view (b) Top-view of the a-Si:H PIN diode.

### 4.3 The $J$ - $V$ Characteristics of a-Si:H Solar Cells

Figure 21 shows the  $J$ - $V$  curves of solar cells with optimized  $n^+$  and  $p^+$  films with 2 mm of pattern size in the dark and under the solar light illumination. The  $n^+$  layer is 30 nm deposited in the condition of  $\text{SiH}_4/\text{PH}_3$  (6.88% in  $\text{H}_2$ )/ $\text{H}_2$  60/20/1000 sccm, 300 W, 800 mT, and 250°C with the lowest resistivity of 94.23  $\Omega$ -cm. The  $p^+$  layer is 30 nm deposited in the condition of  $\text{SiH}_4/\text{B}_2\text{H}_6$  (2% in  $\text{H}_2$ )/ $\text{H}_2$  35/100/400 sccm, 500 W, 450 mT, and 250°C with the lowest resistivity of 202.51  $\Omega$ -cm. The  $i$ -layer is 200 nm deposited in the condition of  $\text{SiH}_4$  50 sccm, 100 W, 400 mT, and 250°C. The gate voltage  $V_g$  was swept from -2 V to 2 V, and figure 21 is the enlargement of the region of -0.5 V to 1 V. Under the solar light illumination, the curve passes through the 4<sup>th</sup> quadrant, and hence the device can deliver power [12]. In the negative bias region (3<sup>rd</sup> quadrant), the current density under illumination is about two order of magnitude larger than that in the dark. Besides,  $J$  saturated quickly in the negative bias under the illumination, this saturation shows that the electric field is strong enough to separate all the electron-holes pairs generated in the  $i$ -layer contributing to the photocurrent. In the positive bias region (1<sup>st</sup> quadrant), electrons from  $n^+$  contact and generated by the illumination are diffused to  $p^+$  contact. The current density under illumination is higher than in the dark.

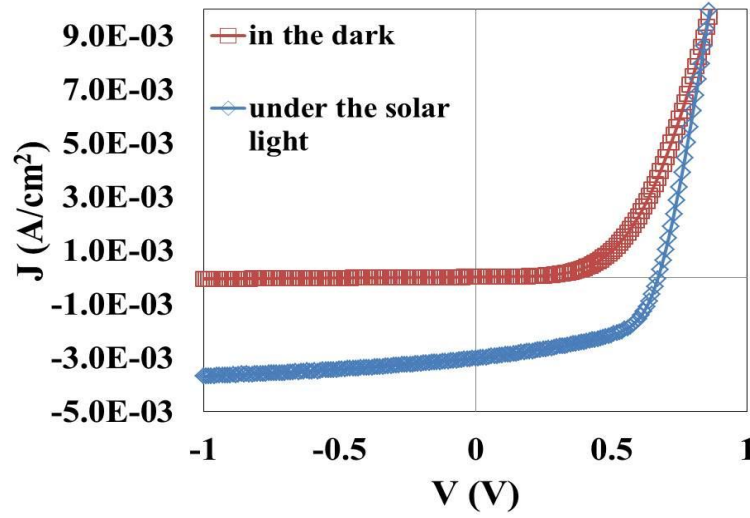


**Figure 21.** The  $J$ - $V$  curves of the PIN diode in the dark and under solar light illumination.

Figure 22 shows the band diagrams of the PIN solar cell in the dark and under illumination. The dark IV curve shifts down to negative currents under illumination and keeps its shape. In the dark, the minority carriers drift across the junction, which is called reverse saturation current. At zero bias, the reverse saturation current is exactly balanced by a small flow of majority carriers in the opposite direction, leading to a zero net current. Under forward bias, the net current direction is from  $p^+$  to  $n^+$ . If the junction is illuminated by a photon with  $h\nu \geq E_g$ , additional electron-hole pairs are generated. These photo-generated carriers drift in the depletion region, move to the junction by the electric field, and are collected by the doped contacts, which contributes to the measured current density. The total current is the sum of the photocurrent and the diode current [46]. The general expression for the current produced by a solar cell is [12]

$$I = I_L - I_o \left( e^{\frac{qV}{kT}} - 1 \right) \quad (4.1)$$

Where  $I_o$  is the dark saturation current,  $I_L$  is the photocurrent and is the sum of the light generated current from the three regions ( $n$ -type,  $p$ -type, and the depletion region),  $q$  is the electronic charge,  $k$  is the Boltzmann's constant, and  $T$  is the absolute temperature. At small positive applied voltage, the diode current is negligible and the current is just the short-circuit current,  $I_{SC}$ , which is the current when  $V=0$  in the equation. When the positive applied voltage is high enough and the diode current (recombination current) becomes significant, the solar cell current drops. At open circuit, which is the voltage when  $I=0$ , all the light-generated current,  $I_{SC}$ , flows through the diode, and no current flows through the external circuit. It is the maximum voltage that a solar cell can deliver. The open circuit current can be expressed by [47]

$$V_{OC} = \frac{kT}{q} \ln\left(\frac{I_L}{I_o} + 1\right).$$

The above equation shows that the  $V_{OC}$  depends on the saturation current and the photocurrent. Since  $I_L$  typically has a small variation and  $I_o$  may change by orders of magnitude, the saturation current density is the key effect. Dutta *et al.* reported that  $I_o$  depends on the recombination current in  $p^+/i$  interface and  $i$ -layer [47]. Therefore,  $V_{OC}$  is a measure of the amount of recombination in the device. The decrease of the recombination current can shift the  $V_{OC}$  to a higher voltage.

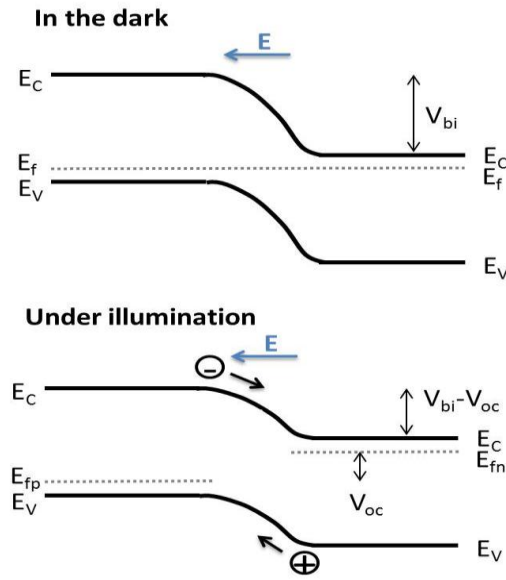


**Figure 22.** Band diagrams of an unbiased p-n junction solar cell in the dark and under illumination [45].

The voltage difference between the two contacts is equal to the splitting of the quasi-Fermi energies. Under the illumination, the photons from the solar spectrum have a broad range of energy, so the electrons are excited to a broad range of energy states in the conductive band. These excited electrons bump into the Si atom and transfer the excess energy to Si atoms. Then, most of the electrons relax to the conductive band edge. Also, the holes are filled up by electrons from the valence band and loss the excess energy until it relaxes to the valence band edge. This “thermalization” process happens quickly, and the electrons stay in the conductive band until they reach the contacts. The energy which can be extracted from each electron is similar to the band gap. It is the thermalized carriers that determine the quasi-Fermi levels. Therefore, the voltage

between the two contacts is maximally as high as the gap energy. The material with a smaller band gap leads to a smaller  $V_{OC}$ , e.g.  $c\text{-Si's } V_{OC} < a\text{-Si's } V_{OC}$  [12, 48].

The point on the  $J$ - $V$  curve where the power produced is at the maximum is referred to as the “maximum power point” with  $V=V_{MP}$  and  $I=I_{MP}$ . The point defines a rectangle area  $P_{MP} = V_{MP}I_{MP}$ , which is the largest rectangle that fits in the  $I$ - $V$  curve. The fill factor, FF, is a measure of the "squareness" of the solar cell and is always less than 1 due to the presence of resistive losses. It is the ratio of the areas of the two rectangles, shown in [12]

$$FF = \frac{P_{MP}}{V_{OC}I_{SC}} = \frac{V_{MP}I_{MP}}{V_{OC}I_{SC}}$$

The power conversion efficiency,  $\eta$ , which is defined as [12]

$$\eta = \frac{P_{MP}}{P_{in}} = \frac{FFV_{OC}I_{SC}}{P_{in}}$$

where  $P_{in}$  is the incident power, which is determined by the incident light's spectrum and intensity. In Figure 21, the intensity of the solar light is fixed at  $1000 \text{ W/m}^2$ . The  $V_{OC}$  is 0.67 V, the  $J_{SC}$  is  $3.01\text{E-}3 \text{ J/cm}^2$ , the  $FF$  is 0.536, and the efficiency is 1.07%.

#### 4.4 The Effect of Cell Size

Figure 23 shows the  $J$ - $V$  curves of solar cells with optimized  $n^+$ ,  $i$ -,  $p^+$  films with 2 mm, 3 mm, 4 mm, 5 mm, 8 mm, and 11 mm of pattern size. The gate voltage  $V_g$  was swept from -2 V to 2 V for the  $J$ - $V$ , and figure 2 is the enlargement of the region of -0.5 V to 1 V. With the increase of pattern size, the area in 4<sup>th</sup> quadrant becomes smaller, the  $V_{OC}$  values are the same, and the  $J_{SC}$  values decrease. After photo-generated carriers move vertically to the junction and are collected by the doped contacts, the carriers move in the ITO in the direction towards the probe tip, which is placed in the middle of the pattern. The ITO film has a higher sheet resistance than metal, i.e. ITO 15-20  $\Omega$ /square vs. Mo 0.1-0.3  $\Omega$ /square. Even though the solar cell with a larger pattern size can produce more electron-hole pairs in the depletion region, the carriers far from the probe tip are collected easily due to the high transverse resistance, hence, the lower photo-generated current density [49]. The  $V_{OC}$ , which is affected by the material, defects, and the interface quality, doesn't change with different pattern size [50]. The  $J_{SC}$  drops abruptly with the increase of size, especially from 5 mm to 8 mm, due to the difficulty of carriers' transverse moving. The solar cell with the smallest size, 2 mm, has the highest  $J_{SC}$ ,  $FF$ , and efficiency.

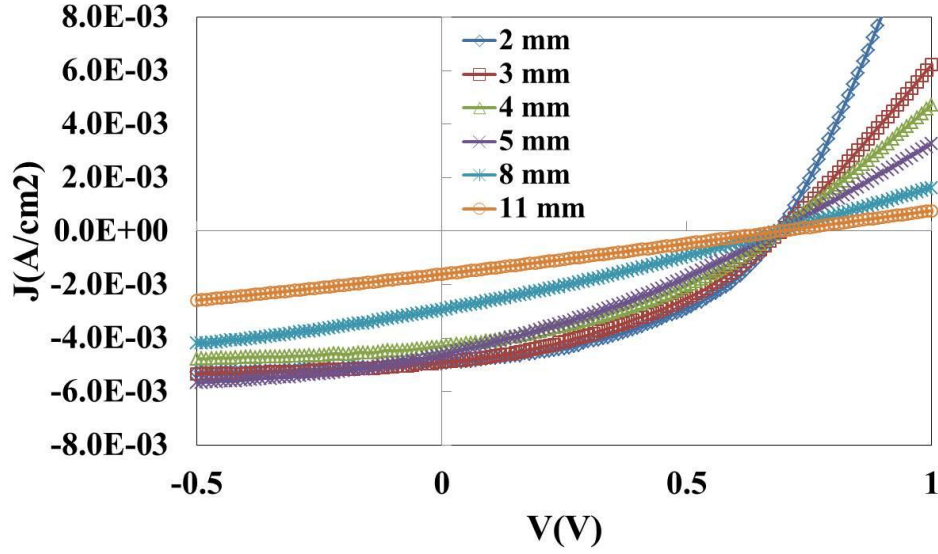


**Figure 23.** The  $J$ - $V$  curves of solar cells with optimized  $n^+$ ,  $i^-$ ,  $p^+$  films with different pattern size under solar light illumination.

#### 4.5 The Effect of the Intrinsic Layer

Figure 24 shows the  $J$ - $V$  curves of solar cell with different  $i$ -layer deposition recipes. The gate voltage  $V_g$  was swept from -2 V to 2 V for the  $J$ - $V$  and figure 24 is the enlargement of the region of -0.5 V to 1 V. The  $n^+$  and  $p^+$  are both 30 nm deposited in the optimized condition. The solar cells with 200 nm  $i$ -layers which are deposited in 80 W/150 mT, 100 W/500 mT, and 200 W/400 mT have smaller  $J$ - $V$  area in 4<sup>th</sup> quadrant and their shape is far from a square. Table 1 shows the  $V_{OC}$ ,  $J_{SC}$ ,  $FF$ , efficiency ( $\eta$ ), shunt resistance ( $R_{Sh}$ ), and series resistance ( $R_S$ ) of each condition. The  $R_{Sh}$  is related to the recombination due to manufacturing defects. Low  $R_{Sh}$  leads to power losses in solar cells by providing an alternate current path for the photo-generated current [12]. Such a



diversion decreases the current flowing through the junction and also decreases the voltage from the solar cell. The  $R_S$  is the series resistance in the solar cell, including the contact resistance between the metal contact and the silicon, and the resistance of the top and rear metal contacts. They can be expressed by a simple circuit model as shown in Figure 25 and the following equation [12]:

$$I = I_L - I_o \left( e^{\frac{q(V + IR_S)}{kT}} - 1 \right) - \frac{(V + IR_S)}{R_{Sh}}$$

$R_S$  has no effect on  $V_{OC}$  since in open-circuit condition the overall current flow through the solar cell and the series resistance is zero. However, near the  $V_{OC}$ , the IV curve is strongly affected by  $R_S$ . An estimate for the value of  $R_S$  can be determined from the slope of the IV curve near the  $V_{OC}$  point. Conversely,  $R_{Sh}$  has no effect on  $J_{SC}$  since the overall flow through the diode. However, the  $J$ - $V$  curve is strongly affected by  $R_{Sh}$  near the  $J_{SC}$ . An estimate for the value of the  $R_{Sh}$  of a solar cell can be determined from the slope of the IV curve near the  $J_{SC}$  point [12].

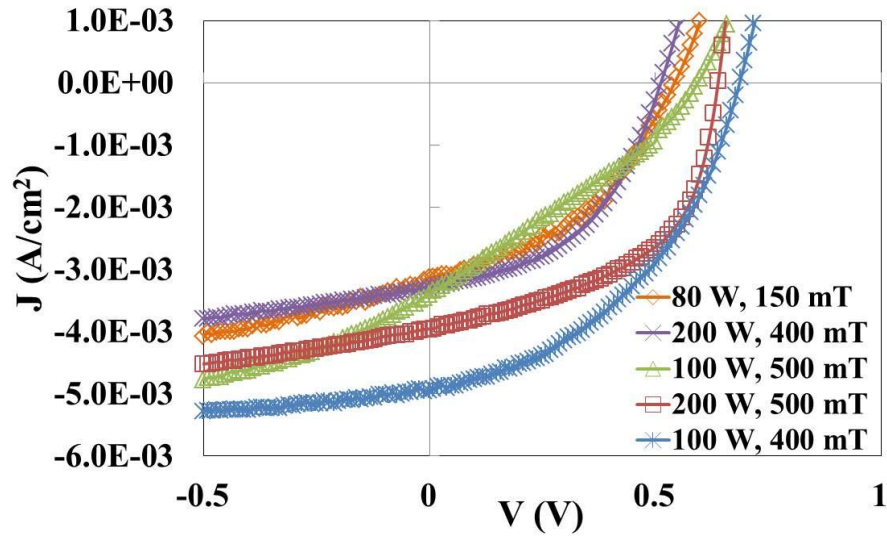


**Figure 24.** The  $J$ - $V$  curves of solar cells with different  $i$ -layers.

| SiH <sub>4</sub><br>flow<br>rate<br>(sccm) | Power<br>(W) | Pressure<br>(mT) | $V_{OC}$<br>(V) | $J_{SC}$<br>(A/cm <sup>2</sup> ) | $FF$  | $\eta$<br>(%) | $R_{Sh}$<br>( $\Omega$ -cm <sup>2</sup> ) | $R_S$<br>( $\Omega$ -cm <sup>2</sup> ) |
|--|--------------|------------------|-----------------|----------------------------------|-------|---------------|---|--|
| 50   | 100          | 400              | 0.68            | 0.00495                          | 0.440 | 1.48          | 625                                       | 38.10                                  |
| 50   | 200          | 400              | 0.51            | 0.00329                          | 0.476 | 0.80          | 533.3                                     | 45.70                                  |
| 50   | 100          | 500              | 0.59            | 0.00340                          | 0.296 | 0.59          | 188.1                                     | 79.70                                  |
| 50   | 200          | 500              | 0.63            | 0.00396                          | 0.529 | 1.32          | 533.3                                     | 19.60                                  |
| 50   | 80           | 150              | 0.54            | 0.00313                          | 0.440 | 0.74          | 228.6                                     | 65.50                                  |

**Table 1.** The  $V_{OC}$ ,  $J_{SC}$ ,  $FF$ , efficiency ( $\eta$ ), shunt resistance ( $R_{Sh}$ ), and series resistance ( $R_S$ ) of the solar cells with different  $i$ -layers.

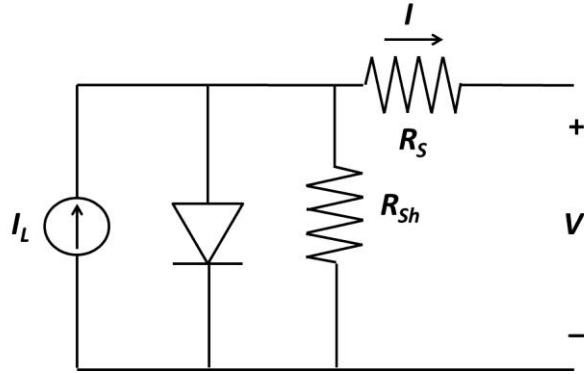


**Figure 25.** Solar cell circuit model including the series and shunt resistances [12].

In Figure 24, the solar cells with *i*-layer which deposited at 80 W/150 mT, 100 W/ 500 mT, and 200 W/400 mT have smaller *J-V* area in the 4<sup>th</sup> quadrant and lower "squareness". Table 1 shows that the solar cells with *i*-layer that deposited at these three conditions have smaller  $R_{sh}$ , which means that more photocurrent is lost due to recombination. The increased possibility of recombination leads to the decrease of  $V_{OC}$ . Therefore, these three solar cells have lower  $V_{OC}$ , about 0.5-0.6 V. The solar cell with *i*-layer deposited at 100 W/500 mT has the largest  $R_s$ , i.e.  $79.7 \Omega\text{-cm}^2$ , which means that the  $n^+/i$ - interface,  $p^+/i$ - interface, and *i*-layer itself have the highest resistance among those samples. The *i*-layer is the main layer to absorb the light and produce photo-generated current. Many, but not all, of the properties of a-Si films are directly related to the presence of hydrogen bonded [51]. The electrical properties of a-Si:H depend on a number of factors such as deposition temperature, power, pressure, and gas flow rate. In Figure 24, the temperature is fixed at 250°C and the  $\text{SiH}_4$  flow rate is fixed at 50 sccm. The annealing temperature is fixed at 200°C because the hydrogen content of these films

is relatively stable when the annealing temperature is below the deposition temperature. The varying factors are power and pressure, which change the concentration of  $\text{SiH}^*$  and  $\text{H}^*$  radicals in the plasma, hence, change the hydrogen content in the film. In addition, compared the condition of 100 W/400 mT and 200 W/500 mT, the 100 W/ 400mT cell has the higher efficiency and  $J_{SC}$  but lower FF. This might be due to the fact that higher  $R_s$  of the 100 W/400 mT cell increases the photo-generated current loss, leading to the lower “squareness” of the  $J$ - $V$  curves. However, the plasma is more stable during the PECVD deposition in 100 W/400 mT. The reflective power of the PECVD during deposition is difficult to control with low gas flow rate and high pressure. The optimized  $i$ -layer deposition condition is  $\text{SiH}_4$  50 sccm, 100 W, 400 mT, and 250°C.

The concentration of H and the binding mode of H and Si are important for both the collection efficiency and light degradation. This is because the H concentration determines the optical band gap that affects the absorption coefficient. The abundance ratio  $\text{SiH}_2/\text{SiH}$  affects the degradation ratio. It is generally agreed upon that the recombination of excess photo-generated electron-hole pairs creates metastable defects in the material. The defect states reduce the carrier mobility and cause the degradation of cell performance. The cause of light-induced degradation is not clear yet. The hydrogen, impurities, microvoids, or weak bonds can cause the degradation [52]. Figure 26 shows the relationship between solar cell efficiency and  $\text{H}_\alpha/\text{SiH}^*$  ratio from the information of OES. The efficiency increases with the rise of  $\text{H}_\alpha/\text{SiH}^*$  ratio at the low  $\text{H}_\alpha/\text{SiH}^*$  range and drastically decreases with the rise of  $\text{H}_\alpha/\text{SiH}^*$  ratio at the high  $\text{H}_\alpha/\text{SiH}^*$  range. It is thought that  $J_{sc}$  and  $V_{oc}$  increase because of the enhanced collection probability of the

carriers and the decreased recombination of electron-hole pairs in the interface [53, 54]. The hydrogenation can passivate the dangling bonds, which acts like recombination centers and will deteriorate the  $R_{sh}$  and  $V_{OC}$  in the film. Therefore, the H treatment mainly improves  $R_{sh}$  and  $V_{OC}$ . For example, compare the condition of 100 W/500 mT and 100 W/400 mT, the  $H_\alpha/SiH^*$  ratio increases from 0.0145 to 0.0763. The conversion efficiency increases from 0.59% to 1.48%. The slope near  $J_{SC}$  is smaller in 100 W/400 mT, which means that the  $R_{sh}$  is larger. The  $V_{OC}$  has an abruptly increase from 0.54 V to 0.68 V. In addition, the current of the cell is also enhanced due to better collection efficiency. The slope near  $V_{OC}$  is larger in 100 W/400 mT, which means that the  $R_s$  in 100 W/400 mT is smaller. However, if the H content is too much, it can lead to the coexistence of SiH, SiH<sub>2</sub> and SiH<sub>3</sub> in the film, which lowers the charge carrying capability. As previously mentioned, the increase of  $H_\alpha^*/SiH^*$  indicates less formation of SiH and more formation of SiH<sub>2</sub> due to too much hydrogen in the plasma, leading to the deterioration of film quality with higher resistivity. It is reported that the short lifetime radicals such as SiH<sub>2</sub><sup>\*</sup> generate higher-order-silane related species such as Si<sub>2</sub>H<sub>6</sub> and Si<sub>3</sub>H<sub>8</sub>, which increases the amount of dangling-bond and microvoid in the film [7]. Voids reduce the light absorption in the film and lead to the increase of  $E_g$  [55]. Therefore, the efficiency drastically decreases with the increase of  $H_\alpha/SiH^*$  ratio at the high  $H_\alpha/SiH^*$  range. The hydrogen content in the *i*-layer should be optimized to a proper concentration.

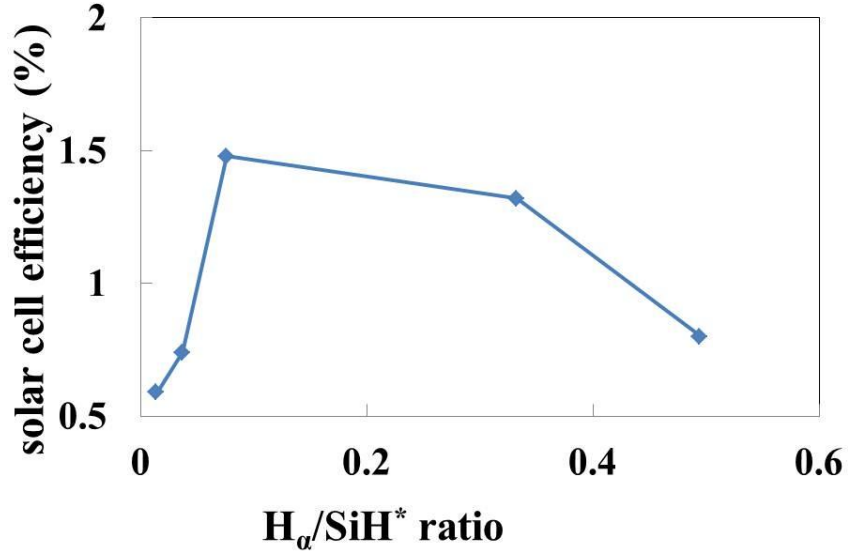


**Figure 26.** The efficiency of solar cells with different *i*-layers vs. the  $H_a/SiH^*$  ratio from OES.

Figure 27 shows the  $V_{OC}$ ,  $J_{SC}$ ,  $FF$ , and efficiency of different thickness of *i*-layers. Those values are normalized to that of the thinnest one (100 nm). The larger current in the thicker *i*-layer is expected because the amount of photo-generated carrier increases as the light penetrates a longer distance in the intrinsic layer and generates more electron-hole pairs. The  $V_{OC}$  values of different *i*-layer thickness are almost constant, which corresponds to the results reported by Guha *et al* that  $V_{OC}$  is constant in some range of thickness [56].  $FF$  has a 13% reduction with a 3-fold increase of thickness. This can be attributed to the reduced electrical field within the thicker devices and thus more strongly voltage dependent photocurrent [57]. It is also reported that the light-

degradation is more serious with the thicker device [57]. Therefore, *i*-layer should be optimized to a proper thickness. The highest efficiency is 2.13% with 300 nm *i*-layer.

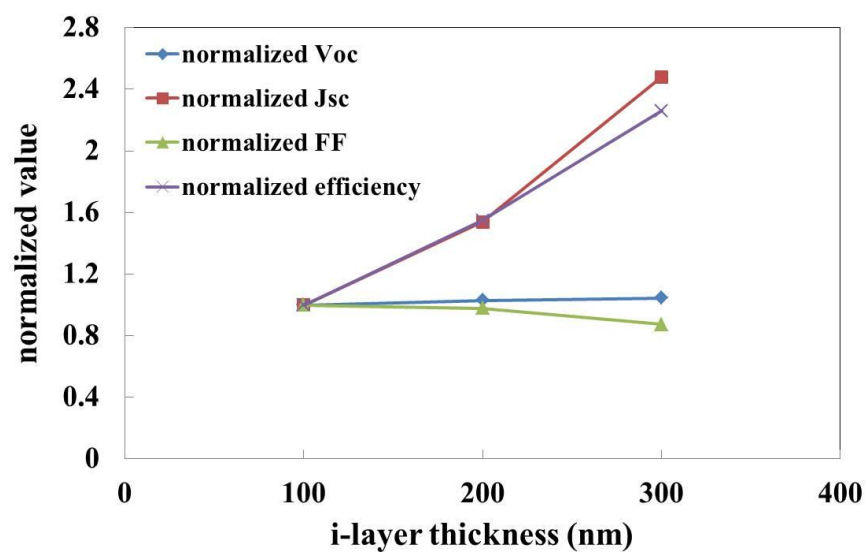


**Figure 27.** The normalized  $V_{OC}$ ,  $J_{SC}$ ,  $FF$ , and efficiency vs. *i*-layer thickness.

## CHAPTER V

### POLYSILICON SOLAR CELL FABRICATION BY MULTIPLE PULSED RAPID THERMAL ANNEALING

#### 5.1 Introduction

This chapter studied the nickel-induced crystallization (NIC) of an amorphous silicon film using the low thermal budget pulsed rapid thermal annealing process (PRTA) with a thin Ni layer and the SiO<sub>2</sub> sacrificial layer. The properties of poly-Si doped layer after PRTA crystallization was studied. In addition, the performance of poly-Si PIN solar cell was also investigated.

#### 5.2 Experimental Method

Figure 28 shows an example of the process flow. The 30 nm thick a-Si:H thin film was deposited by PECVD at 13.56 MHz RF on the corning 1737 gas substrate pre-coated with the sputter deposited Mo (300nm)/Ni (1 nm) stack. The molybdenum was deposited using 20 sccm Ar at 5 mT and 100 W, and the nickel was deposited using 20 sccm Ar at 5 mT and 80 W. The sample was oxidized with a solution composed of H<sub>2</sub>O<sub>2</sub> and H<sub>2</sub>SO<sub>4</sub> (50:50) for 30 sec at room temperature. Then, the sample was dehydrogenated with N<sub>2</sub> at 500°C in the furnace for 5 hr. The crystallization process was carried out with 10-pulsed PRTA process under N<sub>2</sub> purge. Each pulse was composed of 1-sec 850°C heating and 5-sec cooling. During the PRTA process, the glass substrate was loaded on the silicon wafer. The temperature on the backside of the wafer was measured during the



PRTA process, so the temperatures mentioned here was the reference temperature. The glass substrate remains flat without cracking after PRTA. Then, the surface  $\text{SiO}_2$  was stripped off with a 2% dilute HF solution, which removed the surface Ni and prevent the contamination for the subsequent deposition. For the multiple PRTA process, the solution oxidation, PRTA, and oxide stripping steps were repeated for a number of times. The poly-Si films were characterized with X-ray diffraction spectroscopy (XRD), Raman spectroscopy, and 4-point probes.

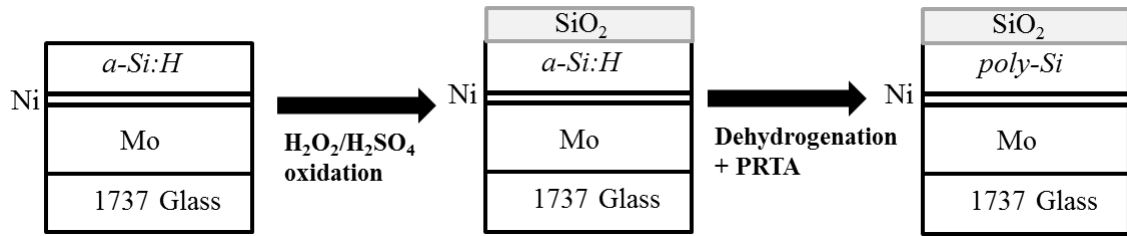


**Figure 28.** Process flow of the  $a\text{-Si:H}$  crystallization by PRTA with a sacrificial  $\text{SiO}_2$

The solar cell composed of glass/Mo (300 nm)/Ni (1 nm)/ $n^+$  (30 nm)/ $i$  (200 nm)/ $p^+$  (20 nm)/ITO (80 nm) was prepared. Four kinds of solar cells were prepared: (1)  $a\text{-Si:H}$   $n^+/i-/p^+$  (2) only  $n^+$  layer treated by NIC, (3)  $n^+/i-$  layers treated by NIC, and (4)  $n^+/i-/p^+$  layers treated by NIC. The  $n^+$  film was deposited at a rate of 12.5 nm/min from  $\text{SiH}_4/\text{PH}_3$  (6.88% in  $\text{H}_2$ )/ $\text{H}_2$  60 sccm/20 sccm/ 1000 sccm, at 300 W, 800 mT, and 250 °C. The resistivity of the  $n^+$  film deposited under this condition is 94.23  $\Omega\text{-cm}$ . The  $i$ -layer films were deposited at a rate of 22.4 nm/min from  $\text{SiH}_4$  50 sccm at 100 W and 400 mT. The  $p^+$  film was deposited at a rate of 22 nm/min from  $\text{SiH}_4/\text{B}_2\text{H}_6$  (2% in  $\text{H}_2$ )/ $\text{H}_2$  35

sccm/100 sccm/400 sccm, 500 W, and 450 mT. The resistivity of the  $p^+$  film deposited under this condition is 202.5  $\Omega$ -cm. Figure 29 shows the process flow. For example, the samples of only  $n^+$  layer treated by NIC were prepared as follows. First, a 30 nm thick  $n^+$  was deposited on Mo/Ni stack. After being oxidized, dehydrogenation, 1<sup>st</sup> cycle (10 pulses) PRTA treated, DHF stripped, being oxidized again, 2<sup>nd</sup> cycle (10 pulses) PRTA treated, and DHF stripped again, the poly-Si  $n^+$  layer was hydrogenated using forming gas (10%/90%  $H_2/N_2$ ) at 400°C for 2 hr to remove defects and passivate dangling bonds in the films. Then, the  $i$  layer and  $p^+$  layer were deposited in one pumpdown in the same chamber without breaking the vacuum. An indium tin oxide (ITO) film was sputter-deposited on top of the PIN stack at a rate of 2 nm/min using 20 sccm Ar at 80 W and 5 mT. The film was patterned into the round-shaped electrodes (2000  $\mu$ m in diameter) by photolithography and etched with the HCl/HNO<sub>3</sub> (3/1 volume) solution. The samples were annealed at 200°C in air for 30 min.

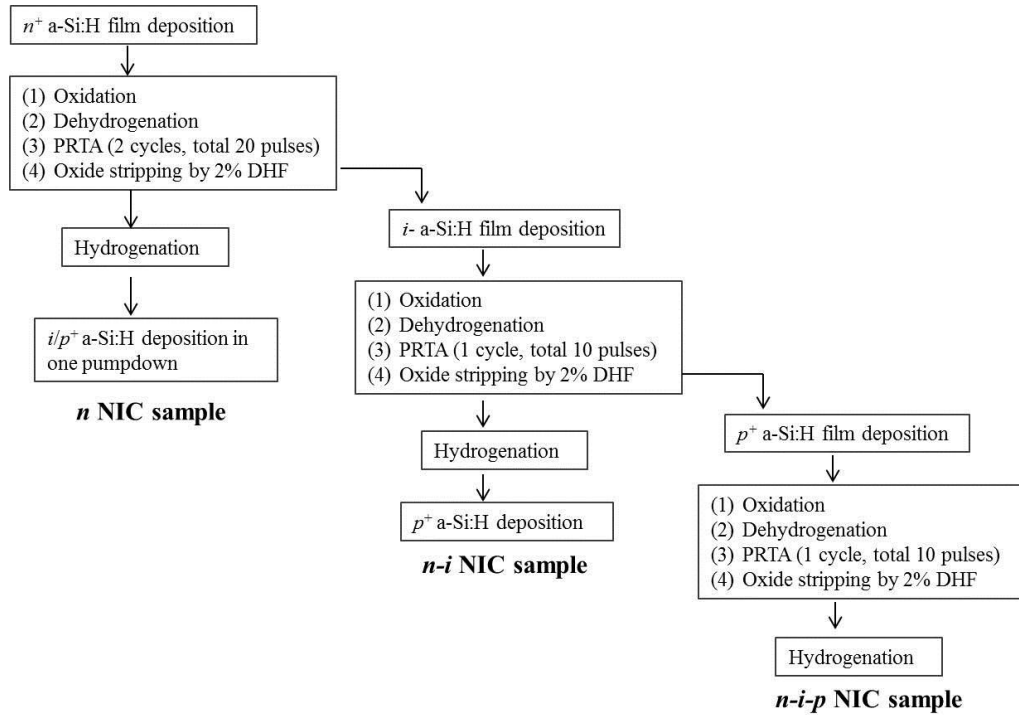


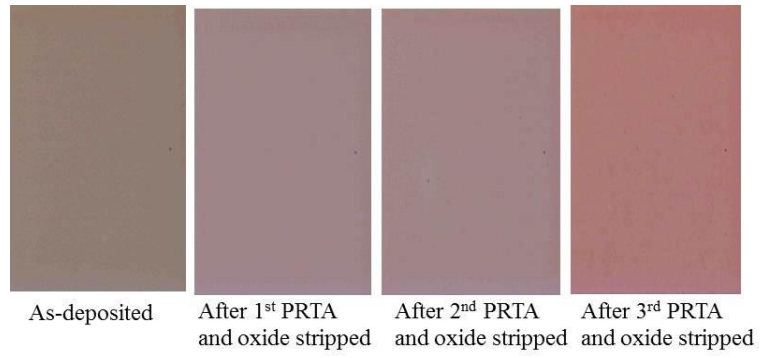
**Figure 29.** Process flow of poly-Si solar cell fabrication.

### 5.3 Nickel-induced Crystallization of a-Si:H Thin Film by Multiple PRTA

Figure 30 shows the microscope pictures taken after every step of  $n^+$ ,  $i^-$ , and  $p^+$  crystallization. The film's color under microscope becomes lighter after crystallization. With the increasing number of time of PRTA, the film color becomes lighter and lighter. In addition, after three times PRTA, some imperfections show on the film. There are two possible reasons for these imperfections. One possible reason is the dehydrogenation resulting pinholes. During PRTA process, the substrate was heated up to 850°C and then immediately cooled down. A lot of hydrogen diffused from the amorphous silicon film in a very short time. As shown by John *et al.* [58], too abrupt dehydrogenation can cause blisters and craters in the film, leading to a non-homogeneous  $pn$  junction. In this case, the posterior deposition of a Transparent Conductive Oxide (TCO), necessary for a solar cell, would short-circuit the junction and make the solar cell unusable. For the experiments in this chapter, a smooth dehydrogenation was done before PRTA. The samples were introduced in the furnace with  $N_2$  environment in room temperature, and heated to 250°C at about 20°C/min then from there up to 500°C at 1°C/min. The samples remained at 500°C for 5 hr, and finally cooled down to room temperature at 5°C/min. In fact, above 350°C, the thermal energy of hydrogen is enough to overcome the Si-H bond energy, and hydrogen is able to diffuse in the a-Si film [59]. The higher the temperature, the faster the hydrogen diffuses. After some time diffusing, a hydrogen

atom would reach the interface with air, and leave to the air. The dehydrogenation should be practically complete after a thermal treatment at 500°C for 5 hr. If not, a lot of hydrogen would abruptly diffuse from the film and cause the pinholes during PRTA process. In addition, c-Si was formed during PRTA process. According to Rao *et al.* [60], when the hydrogen reached the a-Si/c-Si interface, it would aggregate and form bubbles. These bubbles then implode and result in the damage in the film. The higher heating rate causes a greater damage to the film.

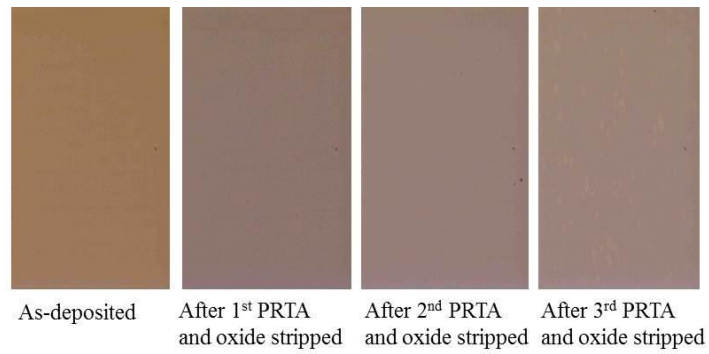
Another possible reason is the change of mechanical properties. During the crystallization process, the amorphous regions around the crystallites will be crystallized until the grain boundaries are formed. Since the crystalline form has a smaller volume than the amorphous form, the stress changes from compressive to tensile due to the shrinking of the material [61]. With more times of PRTA process, the change of mechanical properties becomes more serious, possibly leading to the imperfection in the films.



(a)



(b)



(c)

**Figure 30.** Microscope pictures of Ni-induced crystallization of (a)  $n^+$  (b)  $i^-$  (c)  $p^+$ .

Due to the thickness, i.e. 30nm, and the possible very small fraction of crystalline phase in the PRTA treated a-Si:H films, it's difficult to detect the crystal peaks by XRD pattern. Even after multiple PRTA process, no obvious crystalline Si peak was observed in the XRD pattern. Raman spectroscopy is more powerful to detect the crystalline structure in this kind of thin film. Figure 31 shows the smoothed Raman spectra of five *i*- thin films: as-deposited, after 1-cycle, 2-cycles, 3-cycles, and 4 cycles PRTA. The as-deposited *i*-layer was amorphous because there is no crystalline Si peak. After the PRTA treatment, the Raman spectrum shows an obvious peak between 500 cm<sup>-1</sup> to 520 cm<sup>-1</sup>, which can be deconvoluted into three Gaussian peaks: the peak around 520 cm<sup>-1</sup> represents the TO (transverse optical phonon) mode of single crystalline Si (c-Si), the peak between 510 cm<sup>-1</sup> and 515 cm<sup>-1</sup> indicates the grain boundary in polycrystalline Si (poly-Si), and the broad peak near 490 cm<sup>-1</sup> is contributed by the amorphous phase [18]. Figure 32 shows the smoothed Raman spectra of doped-Si films. The two crystalline peaks in doped-Si film have significant shifts. For the *n*<sup>+</sup> layer, the two crystalline peaks shift to the range of 508-510 cm<sup>-1</sup> and 514-516 cm<sup>-1</sup>. For the *p*<sup>+</sup> layer, the two crystalline peaks shift to the range of 487-492 cm<sup>-1</sup> and 506-511 cm<sup>-1</sup>, and the peaks are also much broader. This shift and broadening of the spectrum are attributed to the smaller grain size in the doped poly-Si than in the intrinsic poly-Si [62, 63]. According to Xia *et al.* [62], the peak shifts 7-20 cm<sup>-1</sup> when the particle size is smaller than 4 nm, and the FWHM of the peak would become broader in about 20- 25 cm<sup>-1</sup>.

The crystallization process was initiated from the formation of crystalline NiSi<sub>2</sub> which has a lattice constant very close to that of the crystalline Si, i.e., 5.406 Å vs. 5.430

Å [64]. The NiSi<sub>2</sub> is acted as nucleation center and then transformed into crystalline Si (c-Si). The diffusion of NiSi<sub>2</sub> through the amorphous Si layer caused the alignment of the atoms to form the crystalline phase [18]. However,  $n^+ - i$ ,  $i - p^+$  interfaces and grain boundaries would trap Ni and NiSi<sub>2</sub> (Ni-related defects), which degrades its electric performance. Therefore, the SiO<sub>2</sub> growth and stripping steps were introduced. It was reported that the H<sub>2</sub>SO<sub>4</sub>/H<sub>2</sub>O<sub>2</sub> treatment could effectively reduce Ni and NiSi<sub>2</sub> that was trapped at the surface [17, 65]. The figure 31 and figure 32 show that the Ni-induced crystallization is applicable to both updoped and doped a-Si films after PRTA treatment even interrupted with the SiO<sub>2</sub> growth and stripping steps. With more times of PRTA treatment, the crystal peak shifts toward the larger Raman frequency. This phenomenon can be contributed to the increase of grain size with increasing total thermal budget [18].

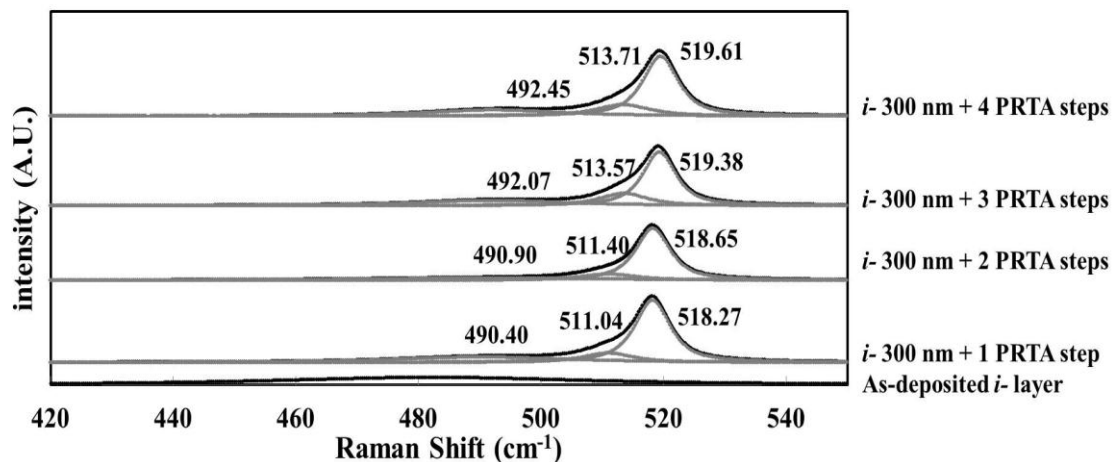
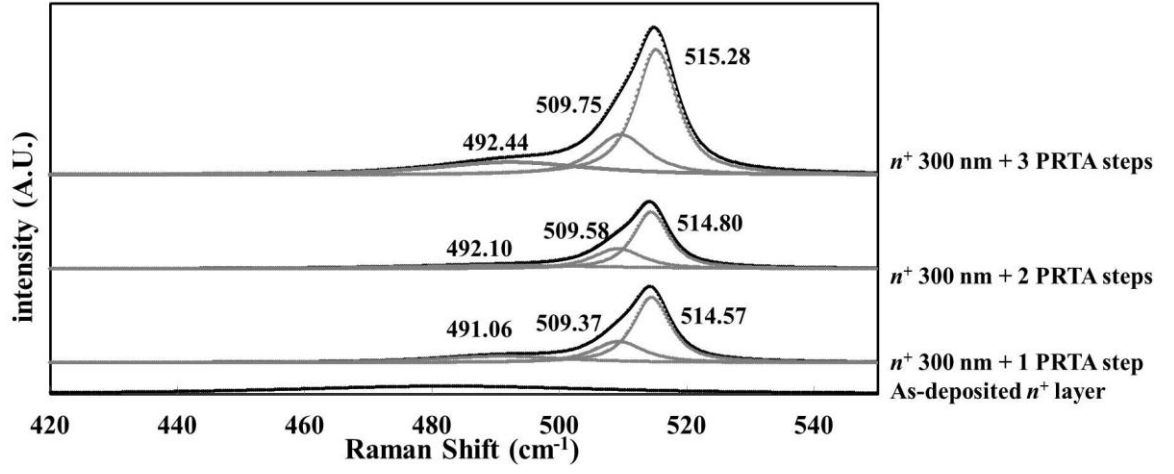
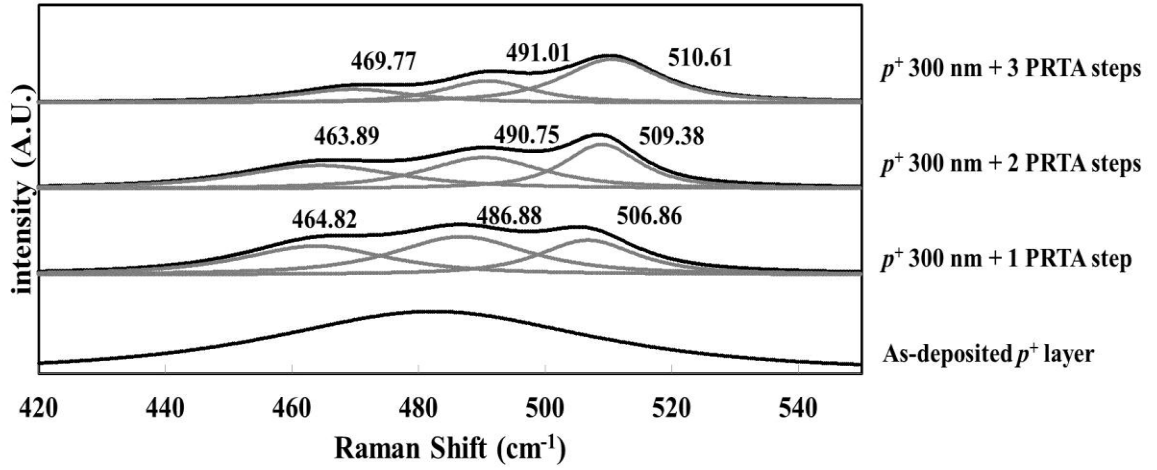


**Figure 31.** Raman spectra of as-deposited *i*-layer and the *i*-layers after 1-4 cycles PRTA treatments.





(a)



(b)

**Figure 32.** Raman spectra of (a) as-deposited  $n^+$  layer and the  $n^+$  layers after 1-3 cycles PRTA treatments, and (b) as-deposited  $p^+$  layer and the  $p^+$  layers after 1-3 cycles PRTA treatments.

According to the calculation made upon phenomenological model of Richter *et al.* and Campbell and Fauchet [66-68], the size of nano-crystals ( $L$ ) can be estimated by relation

$$L = 2\pi\left(\frac{2.24}{\Delta\omega}\right)^{\frac{1}{2}} \quad (5.1)$$

where the  $\Delta\omega$  is the position shift between the actual peak frequency and the TO peak frequency for standard single crystalline Si, i.e.  $520 \text{ cm}^{-1}$ . The volume fraction of crystalline phase ( $X_c$ ) was determined from the following equation [18]:

$$X_c = \frac{I_c + I_{GB}}{I_c + I_{GB} + y(L)I_a} \quad (5.2)$$

where  $I_c$ ,  $I_{GB}$  and  $I_a$  are the integrated intensities of the deconvoluted peaks of c-Si, poly-Si (grain boundary), and a-Si, separately, and  $y(L)$  is the ratio of cross-section area between the amorphous and the crystalline phase. The relationship between  $y(L)$  and  $L$  can be expressed by the following equation [18]:

$$y(L) = 0.1 + \exp\left(-\left(\frac{L}{250}\right)\right) \quad (5.3)$$

Table 2 shows the grain size ( $L$ ) and the volume fraction of crystalline phase ( $X_c$ ) of  $n^+$ ,  $i^-$ , and  $p^+$  layer calculated from figure 31 and figure 32. The increase of both  $L$  and  $X_c$  with the increasing times of PRTA treatment is due to more total thermal budget. The non-doped Si samples have larger grain size than that of the doped Si samples. As shown by K. H. Kim *et al.* [69], the reaction's activation energy calculated from XRD peaks would increase due to the existing of dopant, and would further increase with dopant density. It meant that the mechanism of crystallization of doped a-Si may involve a different diffusion limit step. Therefore, both  $p^+$  and  $n^+$  have smaller grain size than that

of  $i$ - Si. The  $X_c$  of  $i$ - Si is much larger than that of  $p^+$  Si, and similar to that of  $n^+$  Si probably due to the higher dopant density in  $p^+$  than that in  $n^+$ . The doped a-Si needs longer time to achieve fully crystallization than non-doped a-Si does.

| sample |               | Raman grain size (nm) | $X_c$ (%) |
|--------|---------------|-----------------------|-----------|
| $p^+$  | 1 cycle PRTA  | 2.59                  | 64.9      |
|        | 2 cycles PRTA | 2.89                  | 67.6      |
|        | 3 cycles PRTA | 3.07                  | 77.9      |
| $n^+$  | 1 cycle PRTA  | 4.04                  | 78.4      |
|        | 2 cycles PRTA | 4.12                  | 79.2      |
|        | 3 cycles PRTA | 4.33                  | 79.6      |
| $i$    | 1 cycle PRTA  | 7.15                  | 72.6      |
|        | 2 cycles PRTA | 8.09                  | 73.9      |
|        | 3 cycles PRTA | 11.94                 | 74.2      |
|        | 4 cycles PRTA | 15.06                 | 75.8      |

**Table 2.** The grain sizes ( $L$ ) and the crystalline volume fraction ( $X_c$ ) of  $p^+$ ,  $n^+$  and  $i$ - Si samples.

Compared the boron-doped samples ( $p^+$ ) phosphorus-doped samples ( $n^+$ ), the  $p^+$  sample exhibits a smaller grain size than the  $n^+$  sample does. The boron (B) is a

substitution atom for Si. It would compete with Ni atoms and make the Ni atom being interstitial atom in Si. The faster diffusion of those interstitial Ni atoms in Si film leads to more formation of NiSi<sub>2</sub> at the interface of a-Si and c-Si [70]. In the crystallization process, the NiSi<sub>2</sub> acts like a nucleation center, which causes the alignment of atoms and transforms the amorphous phase to crystalline phase. More nucleation center on the interface results in smaller grain size because they would crush with each other. The phosphorus (P) has the ability to trap transition metal elements. Some NiSi<sub>2</sub> are trapped and the diffusion of NiSi<sub>2</sub> through a-Si is retarded. Thus, less Ni-silicide comes to the interface and the larger grain size is formed [70, 71].

Table 3 shows the resistivity of the doped samples measured by four point probe. For both the  $n^+$  and  $p^+$  Si films, the sheet resistivity is decreased by 3 orders of magnitude after PRTA process. The samples with the same dopant were deposited from the same batch of PECVD, so the same film thicknesses were expected before crystallization. The thickness slightly decreased after PRTA process since the top solution oxide layer was removed by the dilute HF after crystallization. Since the sheet resistivity is in inverse proportional to the thickness, the sheet resistivity should get higher with the decrease of thickness. However, in this case, the sheet resistivity becomes smaller due to the crystallization. Therefore, the actual resistivity change between a-Si and poly-Si should be even larger, i.e., more improvement of the conductivity.

| Group |               | Sheet resistivity ( $M\Omega$ ) |
|-------|---------------|---------------------------------|
| $p^+$ | as-deposited  | 66.2                            |
|       | 1 cycle PRTA  | 0.087                           |
|       | 2 cycles PRTA | 0.067                           |
|       | 3 cycles PRTA | 0.042                           |
| $n^+$ | as-deposited  | 53.5                            |
|       | 1 cycles PRTA | 0.031                           |
|       | 2 cycles PRTA | 0.020                           |
|       | 3 cycles PRTA | 0.013                           |

**Table 3.** The sheet resistivity of  $p^+$  and  $n^+$  samples.

#### 5.4 Poly-Si Solar Cells Prepared by Nickel-Induced Crystallization

Figure 33 shows the light  $J$ - $V$  characteristics of solar cells with a-Si:H and poly-Si films prepared by nickel-induced crystallization (NIC). The NIC was performed on: (b)  $n^+$ -layer, (c)  $i$ - $n^+$ , and (d)  $p^+$ - $i$ - $n^+$  in the solar cell. For the sample with NIC  $n^+$ -layer, the diode had a good rectifying property. Also, compared to the all a-Si:H solar cell, the one with poly-Si  $n$ -layer had larger photocurrent and higher efficiency. The solar cell with poly-Si  $i$ - $n^+$  layers had a poor rectifying property, and the solar cell with poly-Si  $p^+$ - $i$ - $n^+$  layers did not show rectifying action. As previously mentioned, the  $n^+$ - $i$ ,  $i$ - $p^+$  interfaces and grain boundaries would trap Ni and NiSi<sub>2</sub>. The higher Ni concentration in the  $n^+$ - $i$  and  $p^+$ - $i$  interfaces after NIC would probably degrade the junction properties of the diode. Even though the SiO<sub>2</sub> layer was introduced to reduce the Ni concentration on the  $n^+$ -layer surface, after  $i$ -layer was deposited and crystallized by PRTA, the Ni was trapped again in the  $n^+$ - $i$  interface when the Ni in bulk  $n$ -layer diffuses to  $i$ -layer. The high Ni concentration in  $p^+$ - $i$  interfaces can also be explained by the same reason. Therefore, the solar cell with NIC  $p^+$ - $i$ - $n^+$  showed a short-circuited  $I$ - $V$  curve due to the deterioration of both  $n^+$ - $i$  and  $i$ - $p^+$  interfaces. The solar cell with NIC  $i$ - $n^+$  showed a poor rectifying property due to the deterioration of the  $n^+$ - $i$  interface [71].

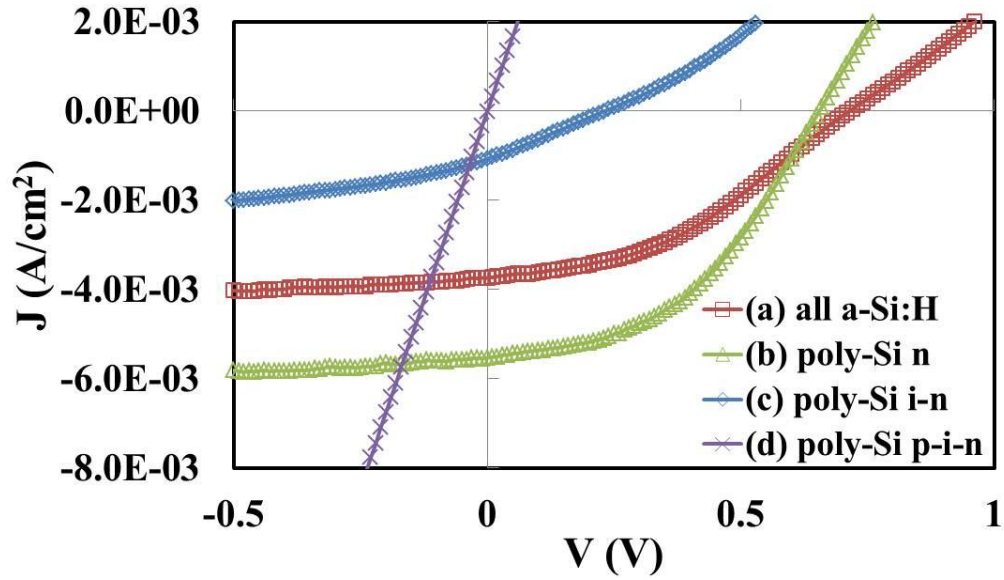


**Figure 33.** J-V curves of solar cells with a-Si:H and poly-Si films prepared by NIC under solar light illumination, (a) all a-Si:H, (b)  $n^+$ -layer crystallized by NIC, (c)  $i-n^+$  layers crystallized by NIC, and (d)  $p^+-i-n^+$  layers crystallized by NIC.

Table 4 shows the cell performance of all a-Si:H and NIC samples. The information of NIC  $p^+-i-n^+$  is not listed since the device did not act like a normal diode. The NIC  $n^+$  sample has lower  $V_{OC}$  and higher  $J_{SC}$  than that of all a-Si:H sample. Because of the lower band-gap of poly-Si (1.1 eV) compared with a-Si:H (1.7-1.9 eV), lower  $V_{OC}$  is achieved in solar cells, but the photocurrent increases by more sufficient absorption of the solar spectrum. The light with longer wavelength and lower energy might be absorbed in poly-Si film due to the smaller band-gap. It was reported that the quantum efficiency of poly-Si was relative high in the long-wavelength region [71].

|             | $V_{OC}$ (V) | $J_{SC}$ (A/cm <sup>2</sup> ) | $FF$  | $\eta$ (%) | $R_{sh}$ ( $\Omega$ -cm <sup>2</sup> ) | $R_s$ ( $\Omega$ -cm <sup>2</sup> ) |
|-------------|--------------|-------------------------------|-------|------------|--|-------------------------------------|
| all a-Si:H  | 0.71         | 0.00374                       | 0.399 | 1.06       | 769.2                                  | 130.1                               |
| $n^+$ NIC   | 0.65         | 0.00553                       | 0.453 | 1.63       | 714.3                                  | 51.6                                |
| $i-n^+$ NIC | 0.23         | 0.00107                       | 0.264 | 0.07       | 250                                    | 210.3                               |

**Table 4.** Cell performance of all a-Si:H and NIC samples.

The cell efficiency is also affected by the film resistivity. The poly-Si  $n^+$  has the sheet resistivity which is three order lower than that of a-Si:H  $n^+$  as shown in table 3. Therefore, the contact resistance of the cell should be reduced with the poly-Si  $n^+$ . The Table 4 shows that the series resistance ( $R_s$ ) calculated from the slope near  $V_{OC}$  reduces from 130.1  $\Omega$ -cm<sup>2</sup> to 51.6  $\Omega$ -cm<sup>2</sup> with poly-Si  $n^+$ . A barrier or contact resistance could occur at the  $n^+/i$  interface due to either interface states or contaminants. In NIC  $n^+$  sample, even though the SiO<sub>2</sub> was produced on the surface of  $n^+$  and then removed in order to reduce Ni concentration,  $n^+/i$  interface was not deteriorated because the SiO<sub>2</sub> with Ni trapped was totally removed before a-Si:H  $i$ - and  $p^+$  was deposited. For poly-Si  $i-n^+$  sample, the  $n^+/i$  interface was contaminated by Ni trapping and the junction properties became worse. The series resistance of poly-Si  $i-n^+$  sample was even higher than that of a-Si:H sample.

Another fundamental difference between poly-Si and a-Si is the nature of the charge transport process. Due to the ordered structure of c-Si, the photo-generated electrons and holes move freely in the film, whereas the motion of the charge carriers in



a-Si is hindered by a large density of defects and disordered structure. Therefore, the electron and hole drift mobilities in a-Si are low compared with those in the poly-Si. For solar cell, the relatively poor transport properties of a-Si leads to the short diffusion length of photo-generated electron-hole pairs. According to Werner *et al.* [72], the recombination speed is very low at the c-Si grain boundaries regardless of the small grain size. The low recombination speed is due to the small barrier height at the grain boundaries, which can be guaranteed by the passivation of hydrogen at grain boundary defects. In addition, light-induced degradation of a-Si:H is considered to limit the efficiency of these types of solar cells. Some dangling bonds form under the solar light exposure. The dangling bonds will trapped the free electron and lead to the lower photocurrent. Since the Si-Si bonds in poly-Si are much stronger than those in a-Si, the poly-Si solar cell can achieve higher conversion efficiency and longer carrier lifetime [30]. However, table 3 shows that the shunt resistance ( $R_{Sh}$ ) calculated from the slope near  $J_{SC}$  didn't change too much when  $n^+$  became poly-Si. That is because the main light absorbing layer is *i*-layer, and only part of the light with longer wavelength can achieve  $n^+$  layer. Since *i*-layers of these two samples are both a-Si:H, the  $R_{Sh}$  didn't change a lot. For poly-Si *i-n^+* sample, high concentration of Ni was trapped on the interface and acted like a generation-recombination center, thus the  $R_{Sh}$  dropped seriously, which leads to more leakage current.

Figure 34 shows the  $J$ - $V$  curves of all a-Si PIN diode and poly-Si  $n^+$  under different light illumination condition. In both samples,  $J$  increases with the wavelength of the light, i.e.,  $J_{\text{blue}} < J_{\text{green}} < J_{\text{red}}$ . This is because that light with the longer wavelength can penetrate deeper into the a-Si:H layer than the light with the shorter wavelength [73]. More electron-hole pairs can be generated with the deeper penetration of the light. In dark condition, the a-Si:H sample and poly-Si  $n^+$  sample have similar dark current. Under the light illumination, the difference of short-circuit current between two samples increases with the wavelength of light. For example, the  $J_{SC}$  of poly  $n^+$  sample is 0.03 mA/cm<sup>2</sup> larger than that of a-Si:H sample under blue light illumination, 0.37 mA/cm<sup>2</sup> under green light illumination, and 0.52 mA/cm<sup>2</sup> under red light illumination. The increase in the  $J_{SC}$  is due to the reduced recombination at  $n^+$  and the improved carrier collection probability with lower  $n^+$  conductivity. Because the penetration depth of blue light is short and probably can reach to only  $p^+$  layer and a small part of  $i$ - layer, the crystallization of  $n^+$  didn't affect the blue light absorption as much as those of other lights. With the increase of light wavelength, the light can go deeper to the  $n^+$  layer. The  $J_{SC}$  increases more due to the longer carrier lifetime in  $n^+$  film and smaller band-gap of poly-Si.

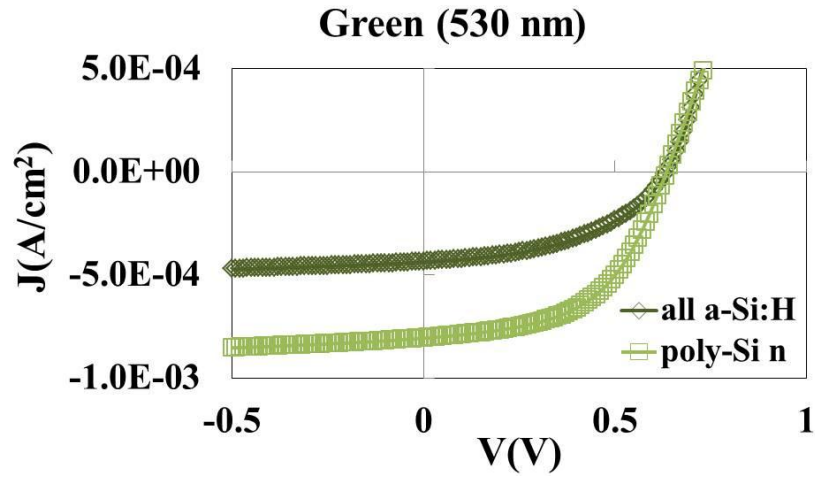
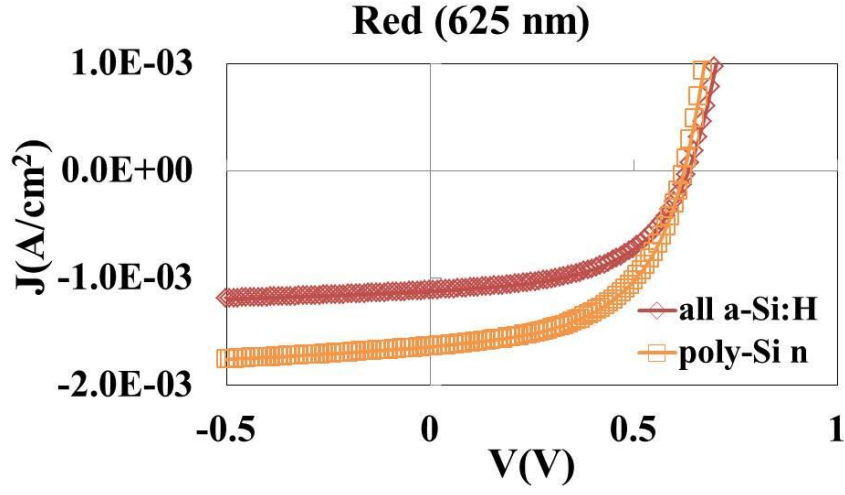


**Figure 34.**  $J$ - $V$  curves of the all a-Si:H diode and the poly-Si  $n^+$  diode prepared by NIC, (a) under red light illumination, (b) under green light illumination, (c) under blue light illumination, and (d) in the dark.

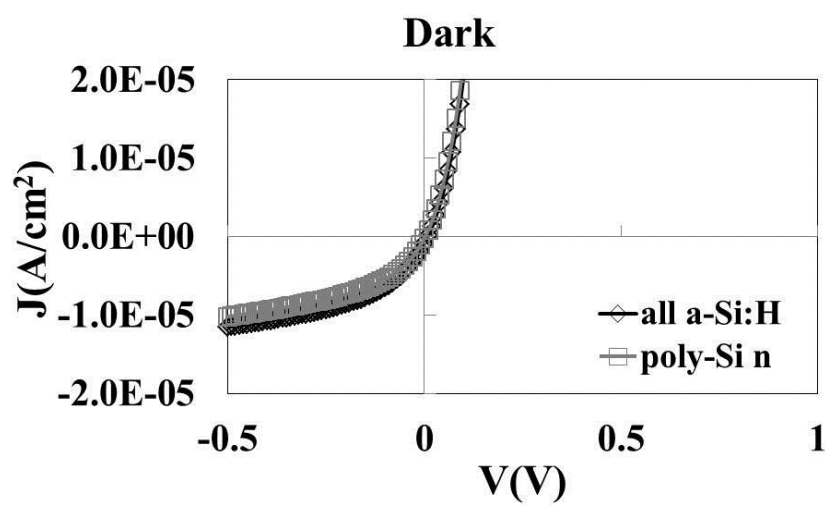
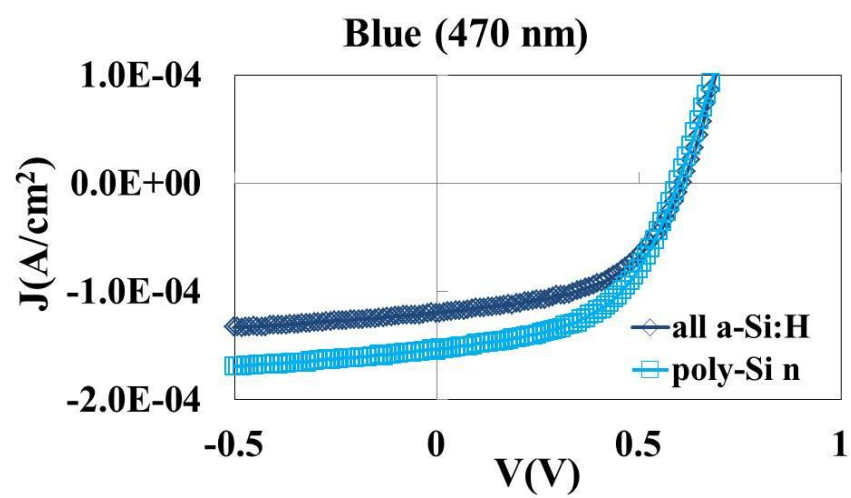


**Figure 34.** Continued.

## CHAPTER VI

### SUMMARY

In this thesis, the power, pressure, and gas flow rate effect on radical intensities ( $\text{SiH}^*$ ,  $\text{H}_\alpha$ ,  $\text{H}_\beta$ ) is studied using OES during a-Si:H PECVD deposition. The relationship among the radical intensities, the deposition rate, and the electrical property of the a-Si:H film is also reported. The  $i$ -,  $n^+$ , and  $p^+$  layers were optimized. The a-Si:H solar cells with optimized  $i$ -,  $n^+$ , and  $p^+$  layers were fabricated and characterized. The pattern size and the thickness of light-absorbed layer ( $i$ -layer) were also determined. In addition, the nickel-induced crystallization were introduced to crystallize a-Si:H to poly-Si. The poly-Si  $i$ -,  $n^+$ , and  $p^+$  layers were successfully crystallized with 70%-80% of crystalline volume fraction by multiple PRTA cycles. The crystallization volume fraction and grain size were calculated using Raman spectra. The application of nickel-induced crystallization on a-Si:H solar cells was also demonstrated. The  $J$ - $V$  curves of poly-Si solar cells were measured in the dark, under solar, red, green and blue light illuminations.

For undoped a-Si:H ( $i$ -layer), the intensities of  $\text{SiH}^*$ ,  $\text{H}_\alpha^*$ ,  $\text{H}_\beta^*$ , and  $\text{H}_2$  increase with the increase of power, and the power effect is more evident in high pressure. When the power is low or the pressure is high, only the  $\text{SiH}^*$  is detected, and the intensity of  $\text{SiH}^*$  is much lower than that in other conditions. The a-Si:H films deposited in this condition has weak Si-Si and unsaturated dangling bonds due to the lack of hydrogen passivation. However, if the hydrogen concentration is too high, the serious positive ion bombardment causes a less dense a-Si:H network with void. The deposition rate

increases with the increase of  $\text{SiH}^*$  intensity. The rise of pressure leads to the competition of increasing  $[\text{SiH}_4]$  and decreasing electron density above threshold energy. Therefore, the dependence of radical intensity on pressure should not have a single trend in this case. The  $\text{SiH}^*$  increases with the rise of power in high pressure condition, and decrease with the rise of power in low pressure condition.

For doped a-Si:H ( $n^+$  and  $p^+$  layers), all intensities increase with the rise of power. The  $\text{H}_\alpha^*/\text{SiH}^*$  ratio also increases with the rise of power, and the  $\text{H}_\beta^*/\text{H}_\alpha^*$  ratio (electron temperature) doesn't change. Therefore, the power mainly contributes to the increase of the electron density for doped a-Si:H layers. The film resistivity is related to the  $\text{H}_\alpha^*/\text{SiH}^*$  ratio. The moderate amount of hydrogen incorporation into a-Si is essential. However, heavy hydrogen dilution gives depletion effects on  $\text{SiH}_4$ , leading to the deterioration of the film. For example, in moderate hydrogen dilution ( $d_H = 14$ ),  $\text{H}_\alpha^*/\text{SiH}^*$  ratio increases with the rise of power. The dangling bonds are passivated and weak Si-Si bonds are etched in this moderate hydrogen dilution. The film is enhanced and the resistivity decreases with the rise of power. However, in high hydrogen dilution condition ( $d_H > 17$ ),  $\text{H}_\alpha^*/\text{SiH}^*$  ratio also increases with the rise of power, leading to more  $\text{SiH}_2$  formation and less  $\text{SiH}^*$  formation, which results in a deteriorated film with high defect density.

With the rise of hydrogen dilution in the feed stream ( $d_H = 17-100$ ), the  $\text{H}_\alpha/\text{SiH}^*$  ratio increases, reflecting the increasing concentration of atomic hydrogen. The deposition rate decreases due to the Si-Si bond etching. Heavy hydrogen dilution gives depletion effects on  $\text{SiH}_4$  by hydrogen abstraction reaction, and short-lifetime species

such as SiH<sub>2</sub> near the electrode contributed dominantly on the film growth, leading to the increase of resistivity.

With the rise of pressure, the intensity of SiH\* is determined by a balance between the increased SiH<sub>4</sub> partial pressure and reduced electron temperature. The intensity of atomic hydrogen is determined by a balanced between the increased partial pressure and the consumption due to abstraction reaction. The H<sub>β</sub>/H<sub>α</sub> ratio decreases a little which indicates the reduced electron temperature due to the increasing number of collisions. The effect of pressure on H<sub>α</sub>/SiH\* ratio is complicated and does not have a single trend. The minimum resistivity can be obtained by changing the parameter toward lower H<sub>α</sub>/SiH\* ratio. The lowest resistivity of  $n^+$  is 94.23 Ω-cm which is obtained under the condition of SiH<sub>4</sub>/PH<sub>3</sub> (6.88% in H<sub>2</sub>)/H<sub>2</sub> 60/20/1000 sccm, 300 W, 800 mT, and 250°C. The lowest resistivity of  $p^+$  is 202.51 Ω-cm which is obtained under the condition of SiH<sub>4</sub>/B<sub>2</sub>H<sub>6</sub> (2% in H<sub>2</sub>)/H<sub>2</sub> 35/100/400 sccm, 500 W, 450 mT, and 250 °C.

Since the resistivity of undoped layers (*i*-layers) was too high to be measured, the *i*-layer was optimized by assembling it with  $n^+$  and  $p^+$  to a PIN diode and measuring the *I*-*V* characterization under solar light illumination. The efficiency increases with the rise of H<sub>α</sub>/SiH\* ratio at the low H<sub>α</sub>/SiH\* range and drastically decrease with the rise of H<sub>α</sub>/SiH\* ratio at the high H<sub>α</sub>/SiH\* range. The hydrogenation can improve the R<sub>Sh</sub> and V<sub>OC</sub> by passivating the dangling bonds, which acts like recombination centers in the film. The current of the cell is also enhanced due to better collection efficiency. However, too much H content leads to the coexistence of SiH, SiH<sub>2</sub> and SiH<sub>3</sub> in the film. The increase of H<sub>α</sub>\*/SiH\* indicates less formation of SiH and more formation of SiH<sub>2</sub> in the plasma,

leading to the formation of higher-order-silane related species such as  $\text{Si}_2\text{H}_6$  and  $\text{Si}_3\text{H}_8$ , which increases the amount of dangling-bond and microvoid in the film. The hydrogen content in the *i*-layer should be optimized to a proper concentration. The optimized *i*-layer with highest efficiency is obtained under the condition of  $\text{SiH}_4$  50 sccm, 100 W, 400 mT, and 250 °C. The smaller the pattern size, the higher the efficiency. In addition, with the *i*-layer thickness increases from 100 nm to 300 nm, the  $J_{SC}$  increases because the amount of photo-generated carrier increase as the light penetrates a longer distance in the intrinsic layer and generates more electron-hole pairs. The  $V_{OC}$  values of different *i*-layer thickness are almost constant.  $FF$  decreases due to the reduced electrical field within the thicker devices and thus more strongly voltage dependent photocurrent. The highest efficiency is 2.13% with 300 nm optimized *i*-layer.

The poly-Si *i*-,  $n^+$ , and  $p^+$  films were successfully obtained by nickel-induced crystallization. More times of PRTA cycles leads to higher crystalline volume fraction and larger grain size, but also higher possibility of imperfection in the film. The  $X_c$  of *i*-Si is much larger than that of  $p^+$  Si, and similar to that of  $n^+$  Si probably due to the higher dopant density in  $p^+$  than that in  $n^+$ . The doped a-Si needs longer time to achieve fully crystallization than non-doped a-Si does. Both  $p^+$  and  $n^+$  have smaller grain size than that of *i*-Si. Besides, the  $p^+$  sample exhibits a smaller grain size than the  $n^+$  sample does. The boron atoms compete with Ni in the film and make the Ni atom being interstitial in Si, leading to more formation of  $\text{NiSi}_2$  at the interface of a-Si and c-Si, and thus smaller grain size. The phosphorus atoms have the ability to trap transition metal elements, leading to the reduction of  $\text{NiSi}_2$ , and thus the larger grain size. For both the  $n^+$



and  $p^+$  Si films, the sheet resistivity is decreased by 3 orders of magnitude after PRTA process.

The application of PRTA crystallization on  $n^+$  of solar cells improves the efficiency. The solar cell with poly-Si  $n^+$  layer had a higher efficiency than all that of a-Si:H solar cell. The photocurrent increases by more sufficient absorption of the solar spectrum. The light with longer wavelength and lower energy might be absorbed in poly-Si film due to the smaller band-gap. The contact resistance of the cell is also reduced with the poly-Si  $n^+$  due to its lower resistivity. Besides, due to the ordered structure of c-Si, the photo-generated electrons and holes move freely in the film, whereas the motion of the charge carriers in a-Si:H is hindered by a large density of defects and disordered structure. Therefore, the electron and hole drift mobilities in a-Si:H are low compared with those in the poly-Si. However, the solar cell with poly-Si  $i$ - $n^+$  layers had a poor rectifying property, and solar cell with poly-Si  $p^+$ - $i$ - $n^+$  layers did not show rectifying action. It is because high concentration of Ni was trapped in  $n^+/i$  and  $i/p^+$  interfaces. Even though the  $\text{SiO}_2$  layer was introduced to reduce the Ni concentration on the surface, after  $i$ - and  $p^+$  layer was deposited and crystallized by PRTA, the Ni was trapped again in interface when the Ni in bulk  $n$ -layer diffuses to  $i$ - and  $p^+$ -layer. Under different light illumination condition,  $J$  increases with the wavelength of the light, i.e.,  $J_{\text{blue}} < J_{\text{green}} < J_{\text{red}}$ . The light with the longer wavelength can penetrate deeper into the a-Si:H layer than the light with the shorter wavelength. More electron-hole pairs can be generated with the deeper penetration of the light. Compared with the all a-Si:H and poly-Si  $n^+$  solar cells, the  $J$  improvement is more obvious under

red light illumination since the light can go deeper to the  $n^+$  layer, which is the main difference of these two samples.

## REFERENCES

1. W. E. Spear, P. G. LeComber, *Solid State Commun.*, Vol. 17, p. 1193, 1975.
2. C. R. Wronski, D. E. Carlson, R. E. Daniel, *Appl. Phys. Lett.*, Vol. 29, p. 602, 1976.
3. A. Matsuda, K. Tanaka, *Thin Solid Films*. Vol. 92, p. 171, 1982.
4. D. Mataras, S. Cavadias, D. Rapakoulias, *J. Appl. Phys.*, Vol. 66, p. 119, 1989.
5. A. P. Paranjpe, J. P. McVittie, S. A. Sell, *J. Appl. Phys.*, Vol. 67, p. 6718, 1990
6. T. Kitagawa, M. Kondo, A. Matsuda, *J. Non-Cryst. Solids*, Vol. 266, p. 64, 2000.
7. T. Nishimoto, M. Takai, H. Miyahara, M. Kondo, A. Matsuda, *J. Non-Cryst. Solids*, Vol. 299, p. 1116, 2002.
8. G. Turban, Y. Catherine, and B. Grolleau, *Thin Solid Films*, Vol. 60, p. 147, 1979.
9. A. Matsuda, K. Nakagawa, K. Tanaka, M. Matsumura, S. Yamasaki, H. Okushi, and S. Iizima, *J. Non-Cryst. Solids*, Vol. 35, p. 183, 1980.
10. D. E. Carlson and C. R. Wronski, *Appl. Phys. Lett.*, Vol. 28, p. 671, 1976.
11. R. E. I. Schropp, R. Carius, and G. Beaucarne, *MRS Bulletin*, Vol. 32, p. 219, 2007.
12. A. Luque and S. Hegedus, *Handbook of Photovoltaic Science and Engineering*, Wiley, p. 66, 2003.
13. J. D. Hwang, T. Y. Chi, J. C. Liu, C. Y. Kung, and I. C. Hsein, *Jpn. J. Appl. Phys.*, Vol. 45, p. 7675, 2006.
14. N. H. Nickel, W. B. Jackson, and J. Walker, *Phys. Rev. B*, Vol. 53, p. 7750, 1996.
15. S. W. Lee and S. K Joo, *IEEE Trans. Electron Dev.*, Vol. 17, p. 160, 1996.
16. Y. Kuo, *ECS Proc.*, Vol. 96-23, p. 30, 1996

17. Y. Kuo and P. M. Kozlowski, *Appl. Phys. Lett.*, Vol. 69, p. 1092, 1996.
18. Y. Kuo and C.-C Lin, *Mater. Res. Soc.*, Vol. 1426, p. 269, 2012
19. John L. Vossen and Werner Kern, *Thin Film Processes II*, Academic Press Inc., 1991.
20. Y. Kuo, K. Okajima, and M. Takeichi, *IBM Journal of Research and Development*, Vol. 43, p. 73, 1999.
21. Y. Kuo, *Thin Film Transistors: Amorphous Silicon Thin Film Transistors*, Kluwer Academic Publishers, 2004.
22. C. V. Raman and K. S. Krishna, *Nature*, Vol. 121, p. 501, 1928.
23. S. C. Saha, A. K. Barua, and S. Ray, *J. Appl. Phys.*, Vol. 74, 1993.
24. H. Jia, J.K. Saha, N. Ohse, and H. Shirai, *J. Non-Cryst. Solids*, Vol. 352, p. 896, 2006.
25. K. Saito and M. Kondo, *Phys. Status Solidi A*, Vol. 207, No. 3, p. 535, 2010.
26. S. K. Ram, L. Kroely, S. Kasouit, P. Bulkin, and P. R. Cabarrocas, *Phys. Status Solidi C*, Vol. 7, No. 3-4, p. 553, 2010
27. W. A. Reid and Q. A. Parker, *Mon. Not. R. Astron. Soc.*, Vol. 425, p.355, 2012
28. J. Perrin and J.P.M. Schmitt, *Chemical Physics*, Vol. 67, p.167, 1982
29. Y. Kuo and S. Lee, *Appl. Phys. Lett.*, Vol. 78, p. 1002, 2001.
30. C. C. Tsai, R. Thompson, C. Doland, F. A. Ponce, G. B. Anderson, and B. Wacker, *Mat. Res. Soc. Symp. Proc.*, Vol. 118, p. 49, 1988
31. U. Kroll, J. Meier, and A. Shah, *Appl. Phys.*, Vol. 80, p. 4971, 1996.
32. G. J. Nienhuis, W. J. Goedheer, E. A. G. Hamers, W. G. J. H. M. van Sark and J.

- Bezemer, *J. Appl. Phys.*, Vol. 82, p. 2060, 1997.
33. H. Yang, C. Wu, J. Huang, R. Ding, Y. Zhao, X. Geng, and S. Xiong, *Thin Solid Films*, Vol. 472, p. 125, 2005
  34. M. Kumeda and T. Shimizu, *Jpn. J. Appl. Phys.*, Vol. 19, No. 4, p. L197, 1980.
  35. J. C. Knight, G. Lucovsky, and R. J. Nemanich, *J. Non-Crystalline. Solids*, Vol. 32, p. 393, 1979.
  36. D. Mataras, f. Coutelieris, P. Kounavis and D. E. Rapakoulis, *J. Phys. D: Appl. Phys.*, Vol.29, p.2452, 1996
  37. W. Beyer, H. Wagner, and H. Mell, *Solid State Communications*, Vol. 39, p. 375, 1981.
  38. R. A. Street, *Physical Review Letters*, Vol. 49, p. 1187, 1982.
  39. M. J. Kushner, *J. Appl. Phys.*, Vol. 63, p.2532, 1998.
  40. M. N. van den Donker, B. Rech, F. Finger, W. M. M. Kessels, and M. C. M. van de Sanden, *Appl. Phys. Lett.*, Vol. 87, p. 263503, 2005
  41. A. Canilloas, J. Campmany, J. L. Andujar and E. Bertran, *Thin Solid Films*, Vol. 228, p. 109, 1993
  42. W. E. Spear and P. G. Le Comber, *Philos. Mag.*, Vol. 33, p. 935, 1976.
  43. Y. Kuo, *Appl. Phys. Lett.*, Vol. 71, p. 2821, 1997.
  44. I. S. Lee and Y. Kuo, *Mater. Res. Soc. Proceedings*, vol. 1536, p. 133, 2013.
  45. P. Bhattacharya, *Semiconductor Optoelectronic Devices*, 2<sup>nd</sup> edition, Prentice Hall, 1996.
  46. U. Dutta and P. Chatterjee, *J. Appl. Phys*, vol. 96, p. 2261, 2004.

47. S. M. Sze, *Semiconductor Devices: Physics And Technology*, 2<sup>nd</sup> edition, Wiley, 2001.
48. M. G. Deceglie, V. E. Ferry, A. P. Alivisatos, and H. A. Atwater, *IEEE J. Photovoltaics*, Vol. 3, No. 2, 2013.
49. N. P. Harder, A. B. Sproul, T. Brammer, and A. G. Aberle, *J. Appl. Phys.*, Vol. 94, p. 2473, 2003.
50. P. J. Zanzucchi, C. R. Wronski, and D. E. Carlson, *J. Appl. Phys.*, Vol. 48, p. 5227, 1997.
51. S. Guha and J. Yang, *Appl. Phys. Lett.*, Vol. 61, p. 21, 1992.
52. H. Angermann, *Appl. Surf. Sci.*, Vol. 254, p. 8067, 2008.
53. J. H. Choi, S. C. Roh, J. D. Jung, and H. I. Seo, *Transactions On Electrical And Electronic Materials*, Vol. 14, No. 4, p. 203, 2013.
54. A. A. Kumbhar and S. T. Kshirsagar, *Thin Solid Films*, Vol. 283, p. 49, 1996.
55. S. Guha, J. Yang, A. Banerjee, B. Yan, and K. Lord, *Solar Energy Materials and Solar Cells*, Vol. 78, p. 329, 2003.
56. A. Fantoni, M. Viera, and R. Martins, *Solar Energy Materials and Solar Cells*, Vol. 73, p. 151, 2002.
57. P. John, I. M. odeh, M. J. K. Thomas, M. J. Tricker, J. I. B. Wilson and R. S. Dhariwal, *J. Mat. Sci.*, Vol. 16, p. 1305, 1981.
58. J. L. Pankove, *Semiconductors and Semimetals 21C: Hydrogenated Amorphous Silicon*, Academic Press, p. 287, 1984.
59. R. Rao, F. Kail, and P. Roca i Cabarrocas, *Journal of Materials Science: Materials*

- in Electronics*, Vol. 18, p. 1051, 2007.
60. P. J. French, *Sensors and Actuators A: Physical*, Vol. 99, p. 3, 2002.
  61. H. Xia, Y. L. He, L. C. Wnag, W. Zhang, X. N. Liu, X. K. Zhang, D. Fang and Howard E. Jackson, *J. Appl. Phys.*, Vol. 78, p. 6705, 1995.
  62. V. Paillard, P. Puech, M. A. Laguna, R. Carles, B. Kohn and F. Huisken, *J. Appl. Phys.*, Vol. 86, p. 1921, 1999.
  63. Y. Kawazu, H. Kudo, S. Onari, and T. Arai, *Jpn. J. Appl. Phys.*, Vol. 29, p. 2698, 1990.
  64. Y.-C Chen, Y.-C Chao, and Y.C. Wu, *ECS Trans.*, Vol. 33, p. 165, 2010.
  65. P. Mishra and K. P. Jain, *Phys. Rev. B*, Vol. 62, p.14790, 2000
  66. H. Richter, Z. P. Wang, and L. Ley, *Solid State Commun.*, Vol. 39, p. 625, 1981.
  67. I .H. Campbell and P. M. Fauchet, *Solid State Commun.*, Vol. 58, p. 739, 1986.
  68. K. H. Kim, A. Nathan, J. Jang, *J. Non-Cryst. Soilds*, Vol. 354, p. 2341, 2008.
  69. J. D. Hwang, J. Y. Chang, and C. Y. Wu, *Appl. Surf. Sci.*, Vol. 249, p. 65, 2005
  70. H. Zhang, X. Zhang, G. Hou, C. Wei, J. Sun, X. Geng, S. Xiong, Y. Zhao, *Thin Solid Films*, Vol. 521, p. 17, 2012
  71. S. I. Muramatsu, Y. Minagawa, F. Oka, T. Sasaki, Y. Yazawa, *Solar Energy Materials and Solar Cells*, Vol. 74, p. 275, 2002.
  72. J. Werner and R. Bergmann, *Tech. Dig. 12<sup>th</sup> Int. Photovoltaic Science and Engineering Conf.*, Sapporo, p. 2041, 1999.
  73. S. H. Wu, Y. Kuo, and C. C. Lin, *Mater. Res. Soc. Proceedings*, vol. 1426, p. 199, 2012.